Characterization of Near-Source Ground Motions with Earthquake Simulations

Brad T. Aagaard, John F. Hall, M.EERI, and Thomas H. Heaton, M.EERI

We examine the characteristics of long-period near-source ground motions by conducting a sensitivity study with variations in six earthquake source parameters for both a strike-slip fault (M 7.0–7.1) and a thrust fault (M 6.6–7.0). The directivity of the ruptures creates large displacement and velocity pulses in the forward direction. The dynamic displacements close to the fault are comparable to the average slip. The ground motions exhibit the greatest sensitivity to the fault depth with moderate sensitivity to the rupture speed, peak slip rate, and average slip. For strike-slip faults and thrust faults with surface rupture, the maximum ground displacements and velocities occur in the region where the near-source factor from the *1997 Uniform Building Code* is the largest. However, for a buried thrust fault the peak ground motions can occur up-dip from this region.

INTRODUCTION

The last century has seen a tremendous growth of urban areas in seismically active regions. Only recently have we begun to realize how the shaking within several kilometers of a fault differs from shaking farther away and how this affects the seismic risk. Near-source ground motions containing large displacement and velocity pulses could potentially cause great harm to modern flexible buildings (Heaton et al. 1995, Hall et al. 1995, Hall 1998). The damaging characteristics are only apparent in moderate to large earthquakes, and the sporadic occurrence of such earthquakes makes the task of understanding near-source ground motions difficult. Additionally, the sparse coverage of recording stations limits our ability to capture ground motions close to fault ruptures. The location of the 1992 Landers earthquake in a remote desert area resulted in only one record of near-source ground motion. While this record has been carefully studied (Iwan and Chen 1994), it shows how the ground moved at only one point. Modeling of the long-period ground motions from this event suggests that larger peak velocities occurred farther south along the fault (Wald and Heaton 1994). The 1994 Northridge and 1995 Kobe earthquakes, which occurred near large centers of population where the station coverage is generally more dense, added more near-source records to the database. Ten stations recorded ground motions within five kilometers of the surface projection of the Northridge earthquake rupture (Hall et al. 1995). Additionally, the Izmit and Kocaeli earthquakes in Turkey and the Chi-Chi earthquake in Taiwan yielded more near-source records, but the total number of recorded near-source ground motions remains limited.

As a result, seismologists have relied on simulations to expand the set of ground motions from actual events and to predict the ground motions for hypothetical ones. Researchers have

(BTA) Geologic and Planetary Sciences, 252-21 Caltech, Pasadena, CA 91125
(JFH) Engineering and Applied Science, 104-44 Caltech, Pasadena, CA 91125
(THH) Geologic and Planetary Sciences, 104-44 Caltech, Pasadena, CA 91125

successfully modeled the near-source ground motions at periods of one second and longer from many recent earthquakes. These include, among others, the 1989 Loma Prieta (Wald et al. 1991), 1992 Landers (Wald and Heaton 1994), the 1994 Northridge (Wald et al. 1996), and the 1995 Kobe (Kamae and Irikura 1998, Wald 1996) earthquakes. The source models associated with these simulations provide valuable information for dissecting past earthquakes. Olsen and Archuleta (1996) approximated the Northridge rupture to examine basin and directivity effects. Pitarka et al. (1998) and Hisada et al. (1998) have studied the directivity and basin edge effects for the 1995 Kobe earthquake to explain the zones of concentrated damage. Others have studied near-source ground motion from the perspective of simple models of dynamic rupture which involve modeling the friction sliding on the fault surface (Archuleta and Frazier 1978, Day 1982, Mikumo and Miyatake 1993, Olsen et al. 1997, Inoue and Miyatake 1998, Oglesby et al. 1998, Oglesby et al. 2000a, Oglesby et al. 2000b). Saikia (1993) examined the ground motions at a network of sites in the greater Los Angeles area for a M 7.0 event on the Elysian Park fault. In order to gauge the uncertainty of the motions, he examined several random distributions of slip and found wide variations in the peak accelerations. Similarly, based on the moderate to strong sensitivity of the ground motions to variations in the seismic moment, source rise time, and heterogeneity of the slip distribution for simulations of hypothetical earthquakes on a section of the San Andreas fault, Graves (1998) suggested that appropriate values for the source parameterization are important for realistic predictions of ground motions.

In the future, ground motion simulations will likely play an increasingly important role in the design of engineering projects. It is important to understand the nature of these ground motions, including the variability caused by changes in the seismic source parameters. With these goals, we expand on previous efforts and study the sensitivity of the long-period near-source ground motions on a strike-slip fault and a thrust fault to systematic variations of six earthquake source parameters: rupture speed, peak slip rate, hypocenter location, distribution of slip, average slip, and fault depth. All of the source parameters fall within the ranges found in kinematic source inversions. We also investigate whether the region with the highest near-source factor from the *1997 Uniform Building Code* (ICBO 1997) includes the area with the maximum ground displacements and velocities. Additional results with an expanded explanation of the simulation techniques may be found in Aagaard (1999).

METHODOLOGY

We want to simulate slip on a fault in an efficient manner and compute the ground motions in a given domain. We impose slip on the fault to create the earthquake and use wave propagation to determine the ground motions in the domain. We solve for the displacement time histories in the three-dimensional dynamic elasticity equation, which in index notation may be written as

$$\lambda u_{k,kj}\delta_{ij} + \mu(u_{i,jj} + u_{j,ij}) = \rho\ddot{u}_i, \tag{1}$$

where λ and μ are Lame's constants, u denotes displacement, and ρ denotes mass density. In practice we cannot find closed-form solutions to Equation 1 for geometrically complex media with heterogeneous properties. We must turn to numerical methods, such as the finite-element method, to calculate the displacement time histories. Although several computationally efficient methods have been developed to synthesize ground motions on finite faults with prescribed slip in a layered half-space (Heaton 1995), we use the finite-element method because we want to use the same software for other simulations with dynamic (self-slipping) ruptures

and three-dimensional material properties. As given in most finite-element texts, such as Rao (1999), the dynamic elasticity equation becomes the matrix equation

$$[M]\{\ddot{u}(t)\} + [C]\{\dot{u}(t)\} + [K]\{u(t)\} = \{F(t)\}, \quad (2)$$

where $[M]$, $[C]$, and $[K]$ denote the mass, damping, and stiffness matrices, respectively, and $\{F\}$ is the force vector. As explained below, the damping matrix comes from the boundary conditions.

With constant, diagonal mass and damping matrices, we can efficiently integrate the matrix differential equation with the central-difference scheme. Time-stepping does not require matrix factorization and necessitates only one multiplication of a nondiagonal matrix and a vector per time step; all other operations involve either vectors or diagonal matrices. For stability of the numerical integration, the time step must be less than the time necessary for the fastest traveling wave to propagate between nodes. Additionally, at least ten nodes per wavelength reduce discretization errors to less than five percent for linear elements (Bao et al. 1998). This requirement can be met throughout the domain by using linear tetrahedral elements which allow adjustment of the local element sizes with only a minor impact on the surrounding elements (Bao et al. 1998). Furthermore, for the same discretization error, the stiffness matrix for a mesh with linear tetrahedral elements requires roughly half the memory as that for a mesh with parabolic elements.

We sample the material properties at the centroid of each element. We also assume small strains and rotations everywhere so that linear theory applies. No material damping is added to Equation 1. In order to convert the consistent element mass matrix to the lumped element mass matrix (diagonal matrix), we require that both matrices yield the same inertial forces for rigid body accelerations in any direction. For a stiffness matrix with hundreds of thousands to millions of degrees of freedom, relatively few entries in the matrix are nonzero. Therefore, we choose to store only the nonzero terms in the upper half of the symmetric, sparse stiffness matrix.

We specify the ground surface as free from tractions and create nonreflecting boundaries on the lateral sides and bottom of the domain. Discrete dampers placed at the nodes on the sides and bottom of the mesh prevent propagating waves from reflecting off the boundaries and contaminating the solution inside the domain. If the dampers for the normal degrees of freedom are tuned to the dilatational wave speed and the dampers for the tangential degrees of freedom are tuned to the shear-wave speed, then the boundary completely absorbs plane dilatational and shear waves propagating normal to the boundary. This method also works reasonably well for incident angles other than 90° (Cohen 1980). The above procedure results in a diagonal damping matrix.

In order to model a domain with a volume of $10^5\,\mathrm{km}^3$, we selected the resolution of the finite-element models for simulation of propagation of waves with periods down to 2.0 sec. As a result, we filter all of the displacement and velocity time histories using a fourth-order Butterworth filter with a corner frequency of 0.5 Hz. Ground motions from real earthquakes contain high frequencies, which make a significant contribution to the velocities. For example, the peak velocities of the fault normal components of the Lucerne record from the Landers earthquake and the Takatori record from the Kobe earthquake decrease by 22% and 57%, respectively, when filtered to periods longer than 2.0 sec (D.J. Wald, personal communication). In other words, including the contributions from higher frequencies in the simulated ground motions would increase the peak velocities presented in this paper significantly.

MODEL OF FAULT

To create slip on the fault, we impose a jump in relative displacement in the finite-element model. In other words, we specify the motion of one side of the fault with respect to the other side while allowing propagation of waves across the fault. We accomplish this by incorporating the fault plane into the geometry of the finite-element model. This interior surface gives structure to the finite-element mesh so that no elements straddle the fault plane. Instead, elements on either side share common faces on the fault plane, as illustrated by Figure 1. All nodes on the fault plane have double the usual number of degrees of freedom in order to allow one side to move relative to the other side; each fault node has six translational degrees of freedom arranged such that each side of the fault has three degrees of freedom, as shown in Figure 1.

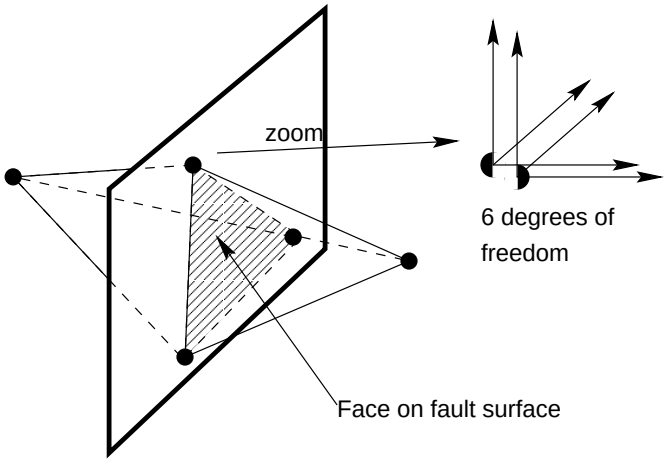

Figure 1. Model of the fault plane in the finite-element mesh. The left portion shows the alignment of the elements on the fault plane. The right portion provides a close-up of a node and its six translational degrees of freedom which allow the sides of the fault to move relative to each other.

Transforming to relative and average degrees of freedom allows explicit control of the relative motion across the fault. We denote the three degrees of freedom corresponding to one side of the fault plane by u_{x_1}, u_{y_1}, and u_{z_1}, and those corresponding to the other side of the fault plane by u_{x_2}, u_{y_2}, and u_{z_2}. We transform the global degrees of freedom to relative and average degrees of freedom using

$$\begin{Bmatrix} u_{x_1-x_2} \\ u_{y_1-y_2} \\ u_{z_1-z_2} \\ u_{x_1+x_2} \\ u_{y_1+y_2} \\ u_{z_1+z_2} \end{Bmatrix} = \frac{1}{\sqrt{2}} \begin{bmatrix} 1 & 0 & 0 & -1 & 0 & 0 \\ 0 & 1 & 0 & 0 & -1 & 0 \\ 0 & 0 & 1 & 0 & 0 & -1 \\ 1 & 0 & 0 & 1 & 0 & 0 \\ 0 & 1 & 0 & 0 & 1 & 0 \\ 0 & 0 & 1 & 0 & 0 & 1 \end{bmatrix} \begin{Bmatrix} u_{x_1} \\ u_{y_1} \\ u_{z_1} \\ u_{x_2} \\ u_{y_2} \\ u_{z_2} \end{Bmatrix}. \tag{3}$$

We do not want to restrict the alignment of the fault plane to any one of the global coordinate planes. Consequently, we rotate from the global coordinate frame to the fault coordinate frame before transforming to the slip degrees of freedom. We prescribe the fault slip by specifying the time histories of the tangential slip degrees of freedom. The normal relative degree of freedom is set to zero at all time steps.

The slip time history gives the progression of slip over time. The slip time history at each point on the fault, $D(x,y,z,t)$, follows the integral of Brune's (1970) far-field time function,

which is shown in Figure 2 and given by

$$\frac{D(x,y,z,t)}{D_\infty(x,y,z)} = 1 - \exp\left(\frac{-(t-t_0(x,y,z))}{\tau(x,y,z)}\right)\left(1+\frac{t-t_0(x,y,z)}{\tau(x,y,z)}\right), \text{ where}$$
$$\tau(x,y,z) = \frac{D_\infty(x,y,z)}{\dot{D}_{max}\, e}. \tag{4}$$

We set the time constant, $\tau(x,y,z)$, that controls the precise time history at each point, based on the specified values of the final slip, $D_\infty(x,y,z)$, and peak slip rate, $\dot{D}_{max}$. Variations in final slip with a uniform peak slip rate produce variations in the slip rise times with longer rise times at points with larger values of final slip. Eighty percent of the slip occurs over a duration of 3.36τ, which is 0.82 sec for a slip of 1.0 m and a peak slip rate of 1.5 m/sec. The speed of the rupture determines the time $t_0(x,y,z)$ at which points on the fault start to slip. We set the rupture speed relative to a constant fraction of the local shear-wave speed.

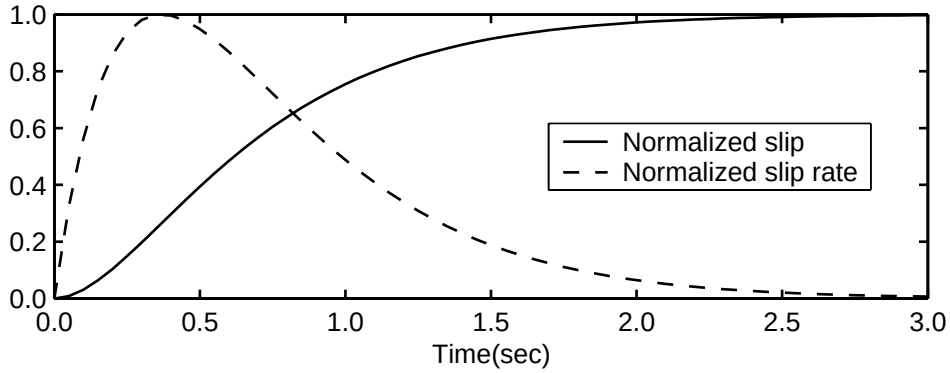

Figure 2. Slip and slip rate as a function of time for the Brune far-field time history function (shown for $t_o = 0$).

We specify the slip at each node on the fault surface. In general, we want a relatively uniform distribution of slip that is tapered at the edges and may or may not contain some degree of heterogeneity. For nonhomogeneous distributions of slip, we begin with circular asperities of various sizes and values, where the overlap among some of the asperities creates patches of slip that vary in both size and shape. On to this we superimpose a homogeneous slip distribution, that is tapered along the buried edges of the fault using an exponential function, in order to produce a desired value of average slip. For homogeneous slip distributions, we follow the same procedure but do not include any asperities.

RESULTS

We want to identify those parameters that most strongly influence the near-source ground motions. We systematically vary the seismic source parameters for both a strike-slip fault and a shallow-dipping thrust fault by selecting different hypocenter locations, peak slip rates, rupture speeds, spatial distributions of the final slip, average slips, and depths of the top of the fault.

STRIKE-SLIP FAULT

The geometry of the strike-slip fault roughly matches the combined fault segments that ruptured in the *M* 7.2 June 1992 Landers event. The 60 km long and 15 km wide vertical fault strikes north in a domain 100 km long, 40 km wide, and 32 km deep as shown in Figure 3.

Figure 4 shows the mass density, shear-wave speed, and dilatational wave speed as a function of depth in the layered half-space. We create the finite-element model at a coarse resolution using the I-DEAS software from the Structural Dynamics Research Corporation, and globally refine the mesh to create the appropriate node spacing. Figure 5 displays a corner of the finite-element mesh at coarse resolution and how we refine each element. The final mesh contains 10 million elements and 6.3 million degrees of freedom. Each simulation took 2.8 hours using 256 processors of the Intel Paragon at the Center for Advanced Computing Research (CACR) at Caltech.

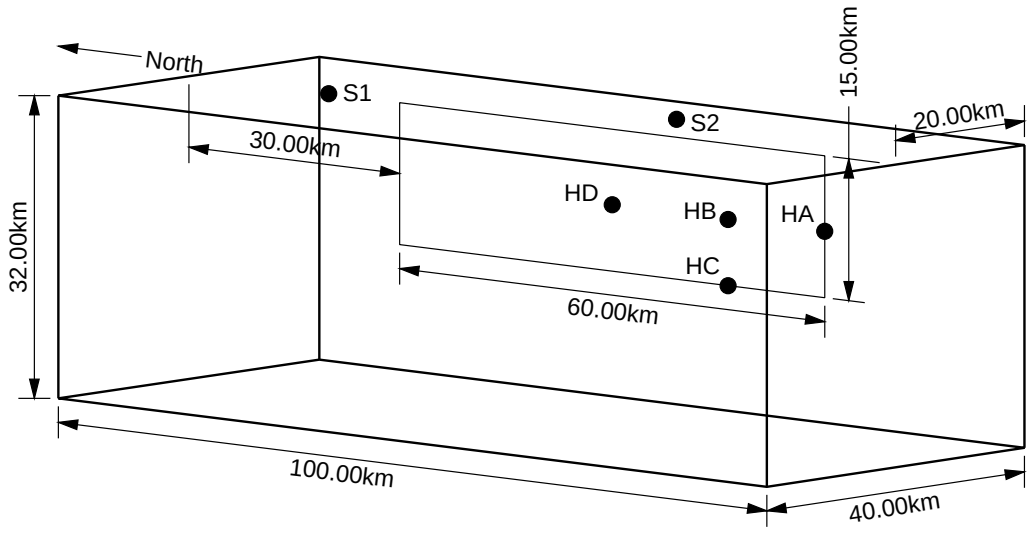

Figure 3. Domain geometry for the strike-slip fault for the case where the top of the fault reaches the ground surface. The labels HA through HD denote the various hypocenter locations. Waveforms are examined at sites S1 and S2.

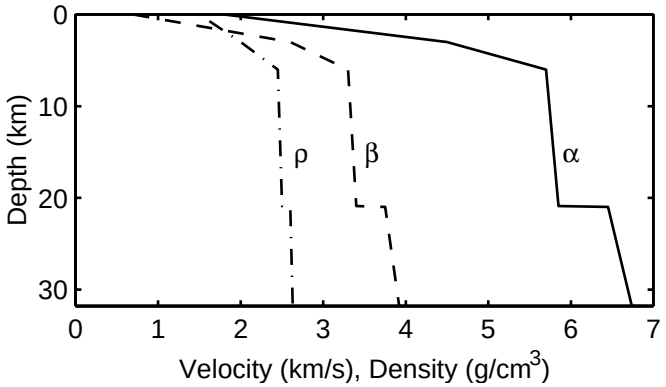

Figure 4. Density (ρ), shear-wave speed (β), and dilatational wave speed (α) as a function of depth in the layered half-space.

Earthquake Source Parameters for the Strike-Slip Fault

Table 1 summarizes the parameters for each scenario. The base case (scenario base) features a homogeneous slip distribution with an average slip of 2.0 m that is tapered on three edges, a rupture speed of 80% of the local shear-wave speed, a peak slip rate of 1.5 m/sec, and a hypocenter located near mid-depth at the south edge of the fault (HA). The four hypocenter locations on the southern half of the fault (labeled HA through HD in Figure 3) sit at a depth of

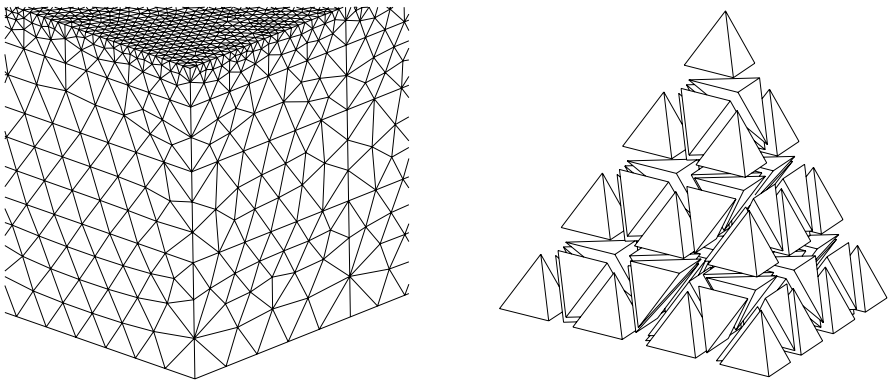

Figure 5. The plot on the left shows a corner of the coarse mesh, and the diagram on the right demonstrates how each element in the coarse mesh is divided into 64 elements to create the refined mesh.

Table 1. Summary of the parameters for the simulations on the strike-slip fault

Scenario	Slip Pattern	Rup. Speed (% of β)	Peak Slip Rate (m/sec)	Hypo. Location	Fault Depth (km)	Avg. Slip (m)	Mom. Mag.
base	homogeneous	80	1.5	HA	0–15	2.0	7.0
vr70	homogeneous	70	1.5	HA	0–15	2.0	7.0
vr90	homogeneous	90	1.5	HA	0–15	2.0	7.0
vs10	homogeneous	80	1.0	HA	0–15	2.0	7.0
vs20	homogeneous	80	2.0	HA	0–15	2.0	7.0
hyB	homogeneous	80	1.5	HB	0–15	2.0	7.0
hyC	homogeneous	80	1.5	HC	0–15	2.0	7.0
hyD	homogeneous	80	1.5	HD	0–15	2.0	7.0
sliptop	weakupper	80	1.5	HA	0–15	2.0	7.0
slipbot	weaklower	80	1.5	HA	0–15	2.0	7.0
sliphet	strongheter	80	1.5	HA	0–15	2.0	7.0
slip3	homogeneous	80	1.5	HA	0–15	3.0	7.1
fault4km	homogeneous	80	1.5	HA	4–19	2.0	7.1
fault8km	homogeneous	80	1.5	HA	8–23	2.0	7.1

8.0 km at the southern edge of the fault plane, the southern quarter point, and the fault center, and at a depth of 15 km at the southern quarter point.

For each simulation we select a rupture speed of 70%, 80%, or 90% of the local shear-wave speed. Additionally, we independently specify a spatially uniform peak slip rate of 1.0 m/sec, 1.5 m/sec, or 2.0 m/sec. The median values of 80% of the shear-wave speed and 1.5 m/sec correspond to a typical average rupture speed and peak slip rate found in inversions of strong ground motions (Heaton 1990). Given our choice of imposing relatively uniform slip, albeit with some random heterogeneity in three scenarios, we choose to keep the peak slip rate uniform over the fault surface because great uncertainty still exists regarding the duration of slip for the very shallow portion of the rupture. Source inversions of the Landers earthquake (Wald and Heaton 1994) and the Kobe earthquake (Wald 1996) inferred slip durations of more than four seconds for the shallow portion of the slip, but eyewitnesses reported slip durations of one second or less for the 1990 Luzon earthquake in the Phillipines (Yomogida and Nakata 1994)

and the 1983 Borah Peak earthquake (Wallace 1984). The TCU052 and TCU068 records from the 1999 Chi-Chi earthquake with maximum horizontal velocities of 1.5 m/sec and 2.0 m/sec (Huang et al. 2000) are consistent with peak slip rates of about $1.5 - 3.0$ m/sec.

The slip distributions include: homogeneous ones that are tapered on the buried edges of the fault, two weakly heterogeneous distributions (weakupper with a bias towards slip near the surface and weaklower with a bias towards slip near the bottom), and a strongly heterogeneous distribution (strongheter which is shown in Figure 6). All of the slip distributions have an average slip of 2.0 m, except for the one in scenario slip3, which has an average slip of 3.0 m. For the heterogeneous distributions, we start with 30 asperities with uniform random distributions of radii, heights, and locations on the fault surface and superimpose a homogeneous distribution to create the desired amount of slip. For the weakly heterogeneous distributions the asperity heights range from -0.25 m to 1.0 m with radii between 5.0 km and 10 km. Similarly, for the strongly heterogeneous distribution the asperity heights range from 0.0 m to 3.2 m with radii between 3.0 km and 8.0 km.

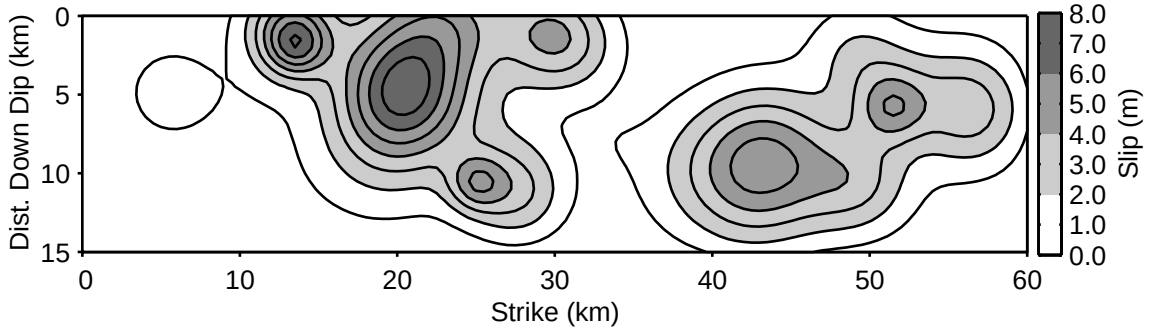

Figure 6. Strongly heterogeneous slip distribution strongheter, which is tapered on three edges with an average slip of 2.0 m and a maximum slip of 7.8 m.

We examine only the base case in detail. For the other simulations, we examine groups of scenarios in order to study the sensitivity of the ground motions to a single parameter. All scenarios with both surface rupture and an average slip of 2.0 m have a moment magnitude of 7.0. Thus, for these scenarios any variability in the ground motions is independent of the moment magnitude.

Strike-Slip Fault Base Case

We start our examination of the base case by considering the free-surface particle velocities which show the propagation of the shear wave and a train of surface waves. Figure 7 gives snapshots in time of the magnitude of the velocity vector at each point on the ground surface. The velocity near the fault increases as the rupture progresses and begins to decrease after the rupture reaches the north end of the fault at about 24 sec. The most severe ground motions are concentrated close to the fault.

The maximum horizontal displacements and velocities on the ground surface (Figure 8) give a clear picture of the effect of directivity on the ground motions. The shear wave has particle motion perpendicular to the fault plane (east-west direction) and builds as the rupture propagates. This leads to a maximum horizontal displacement of 2.2 m at sites 1.7 km east or west of the north end of the fault. The maximum velocity of 2.9 m/sec occurs slightly farther south at sites located 6.7 km south of the north end of the fault and 0.5 km east or west.

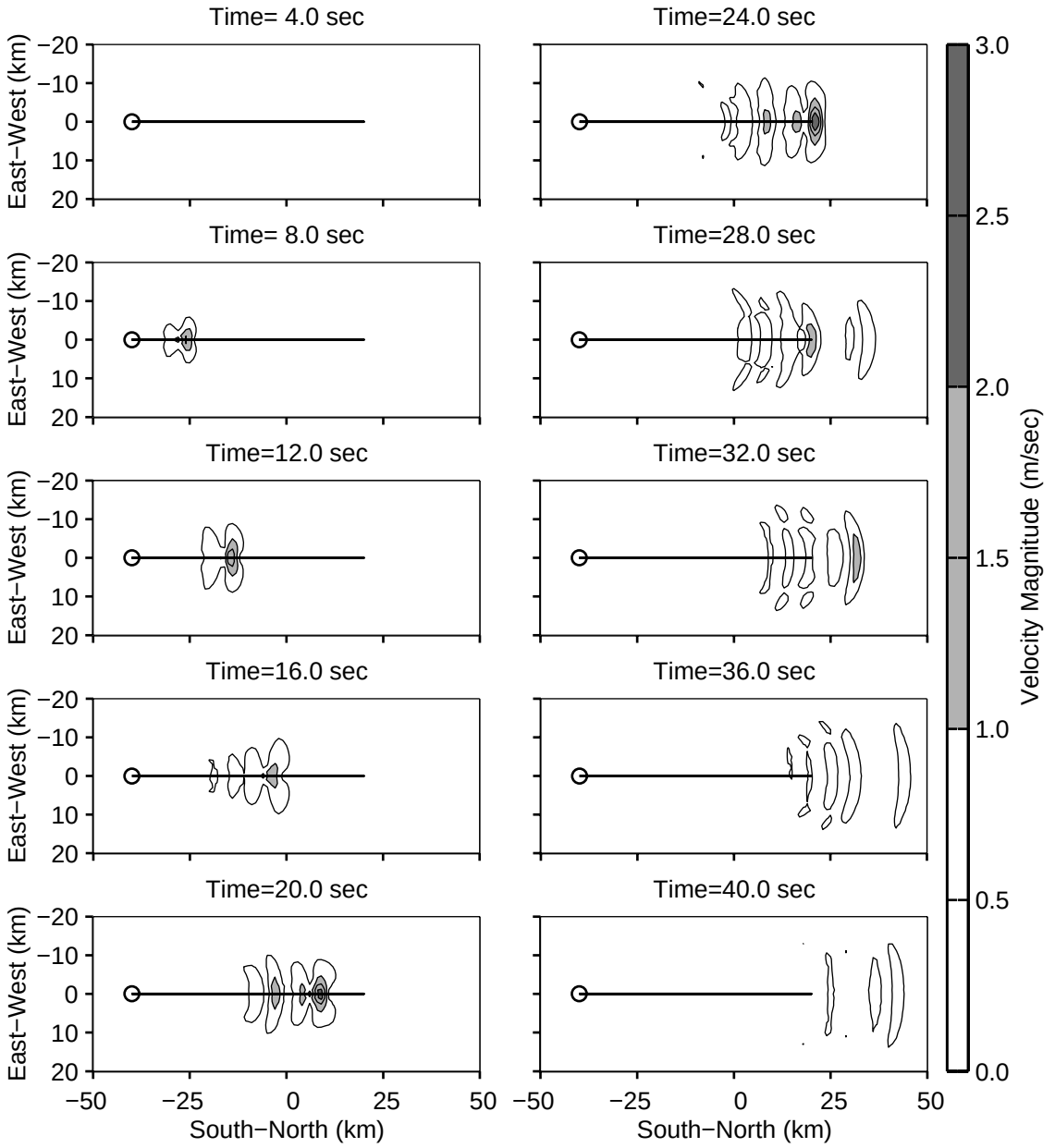

Figure 7. Snapshots of the magnitude of the velocity vector (0.5 Hz low-pass filtered) at each point on the ground surface for scenario base. The solid line indicates the projection of the fault onto the ground surface, and the hollow circle identifies the epicenter.

The maximum velocities exceed 1.0 m/sec over an area of 690 km^2. Since the simulations include only frequencies less than 0.5 Hz, we expect the true peak velocities to be significantly larger. The distribution of maximum horizontal velocities closely resembles the one observed by Archuleta and Frazier (1978), although they found a faster decay in the values past the ends of the fault.

The directivity of the rupture causes large variations in the ground motions with changes in the azimuthal angle between the projection of the slip vector onto the ground surface and the vector from the epicenter to the site. We consider two sites located 10 km from the fault but with azimuthal angles that differ by 18°; the sites are labeled S1 and S2 in Figure 3. Site S1

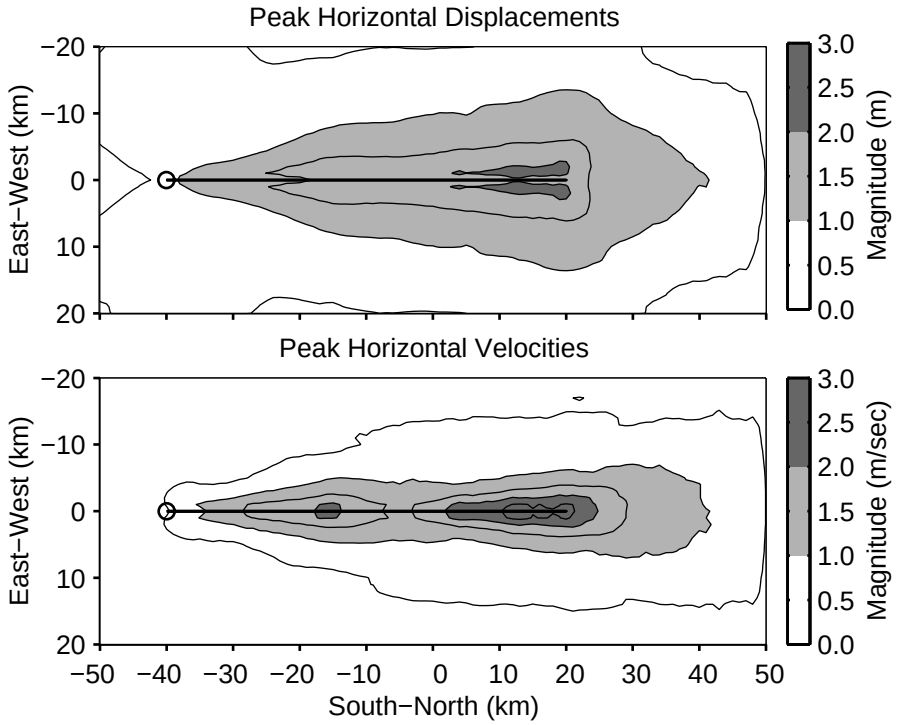

Figure 8. Maximum magnitudes of the horizontal displacement and velocity vectors (0.5 Hz low-pass filtered) at each point on the ground surface for scenario base. The solid line indicates the projection of the fault plane onto the ground surface, and the hollow circle identifies the epicenter.

lies 10 km north of the north end of the fault (azimuthal angle of 0°) and site S2 lies 10 km east of the fault center (azimuthal angle of 18°).

The most important difference between the two sites is the fact that, while both have similar peak horizontal displacements (1.2 m at site S1 and 0.90 m at site S2), the peak horizontal velocity at site S1 is 2.6 times greater than the peak horizontal velocity at site S2 (1.2 m/sec at site S1 versus 0.48 m/sec at site S2). We examine the waveforms in the next section. The directivity effect causes the shear-wave energy from all points on the fault to arrive at nearly the same time at site S1. At site S2 the energy arrives over a longer interval of time which reduces the peak velocity. This leads to much larger ordinates in the acceleration response spectra (Figure 9) at site S1 for periods up to 4.0 sec. The waveforms used for the spectral calculation were rotated into the direction with the maximum peak-to-peak velocity, which roughly coincides with the east-west direction in both cases. In this direction at site S1, the peak acceleration (0.5 Hz low-pass filtered) is 0.25 g. In Figure 9 we also overlay the design spectrum from the *1997 Uniform Building Code* (*UBC*) for a site with soil class S_D in zone 4 that lies within 2 km of a fault designated as source type *A*. For periods greater than 4 sec the computed response spectrum for site S1 falls close to the *UBC* spectrum. However, the peak in the site S1 response spectrum at about 3 sec lies well above the *UBC* spectrum.

Summary of Results for the Strike-Slip Fault

We now consider the fluctuations in the ground motions as the source parameters change. Table 2 provides a simple measure of this variability by giving the overall maximum horizontal

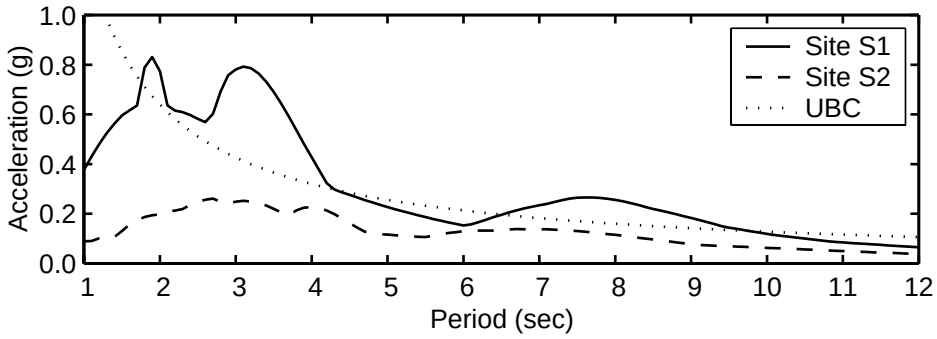

Figure 9. Horizontal acceleration response spectra for 5% critical damping at sites S1 and S2 for scenario base. The ground motions have been low-pass filtered to include periods greater than 2.0 sec. The dotted line indicates the *UBC* design spectrum for a site with soil class S_D in zone 4 that lies within 2 km of a fault designated as source type *A*.

Table 2. Maximum displacements and velocities (0.5 Hz low-pass filtered) at site S1, site S2, and on the ground surface for each strike-slip fault scenario

Scenario	Mom. Mag.	Avg. Slip (m)	Max. Horiz. Disp.			Max. Horiz. Vel.		
			S1 (m)	S2 (m)	surface (m)	S1 (m/sec)	S2 (m/sec)	surface (m/sec)
base	7.0	2.0	1.2	0.90	2.2	1.2	0.48	2.9
vr70	7.0	2.0	1.1	0.85	1.8	0.88	0.46	1.9
vr90	7.0	2.0	1.3	1.0	2.4	1.5	0.63	3.5
vs10	7.0	2.0	0.96	0.80	1.7	0.89	0.38	1.8
vs20	7.0	2.0	1.3	0.96	2.6	1.5	0.58	3.7
hyB	7.0	2.0	1.0	0.78	2.1	1.1	0.39	2.7
hyC	7.0	2.0	0.95	0.76	2.1	1.2	0.36	2.9
hyD	7.0	2.0	0.92	0.89	1.9	1.1	0.48	2.5
sliptop	7.0	2.0	1.1	0.91	2.5	1.2	0.47	2.8
slipbot	7.0	2.0	1.2	0.82	2.1	1.2	0.49	2.9
sliphet	7.0	2.0	1.0	0.95	2.7	1.2	0.42	2.6
slip3	7.1	3.0	1.4	1.2	2.5	1.3	0.57	2.8
fault4km	7.1	2.0	0.90	0.86	1.2	0.88	0.52	1.7
fault8km	7.1	2.0	0.85	0.45	0.95	0.84	0.37	1.0

displacements and velocities observed over the entire ground surface; we also give the maximum displacement and velocity at sites S1 and S2 for each scenario. We refer to these values in the discussion of each group of scenarios associated with a source parameter.

We examine the variability of the ground motions for rupture speeds of 70% of the local shear-wave speed (scenario vr70), 80% of the local shear-wave speed (scenario base), and 90% of the local shear-wave speed (scenario vr90). As the rupture speed approaches the shear-wave speed, the efficiency of the reinforcement of the shear wave increases because the distance between the shear wave and the following rupture front decreases. Comparing the horizontal velocity components at sites S1 and S2 for the three scenarios (Figure 10), we see sharper phase arrivals as the rupture speed increases because at each site the energy from all parts of the fault arrives in a relatively shorter interval of time. Due to the different azimuthal angles, the

distance the rupture propagates towards site S1 is much greater than that for site S2. This leads to a substantial increase in the amplitude of the shear wave with a much larger amplitude at site S1 compared to site S2 (the peak velocities increase from 0.88 m/sec to 1.2 m/sec to 1.5 m/sec at site S1 and from 0.46 m/sec to 0.48 m/sec to 0.63 m/sec at site S2). The amplitudes of the trailing surface waves remain relatively unchanged.

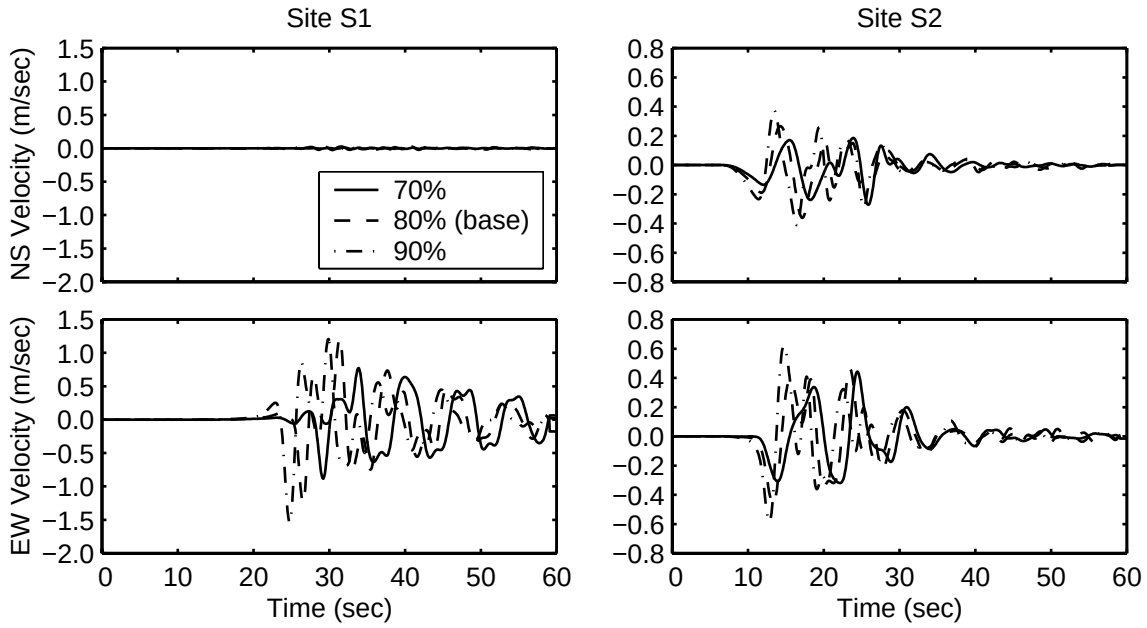

Figure 10. Comparison of horizontal velocity time histories at sites S1 and S2 for the three rupture speeds.

Scenarios vs10, base, and vs20 allow comparison of the ground motions from simulations with peak slip rates of 1.0 m/sec, 1.5 m/sec, and 2.0 m/sec, respectively. As the peak slip rate increases, the slip on the fault occurs over a shorter period of time. This leads to an increase in both the maximum displacements and velocities; the overall maximum horizontal velocity on the ground surface increases from 1.8 m/sec to 2.9 m/sec to 3.7 m/sec for the three cases. While we have considered rupture velocity and peak slip rate (slip duration) independently, crack models from dynamic fracture mechanics (Husseini 1977, Freund 1979, Kanamori and Heaton 2000) and dynamic rupture simulations (Day 1982, Fukuyama and Madariaga 2000) show that these parameters are closely related.

We study the sensitivity of the ground motions to the location of the hypocenter using scenario base (hypocenter HA), scenario hyB, scenario hyC, and scenario hyD. Changing the location of the hypocenter significantly alters the ground motions in some locations but has a minimal impact at other locations. For example, the relative changes in amplitude at site S2 exceed those at site S1 as shown in Figure 11. For each of the four hypocenter locations, site S1 has an azimuthal angle of 0°. Furthermore, site S1 lies far enough away from the hypocenter in all four cases that the amplitude of the shear-wave velocity stabilizes well before it arrives at site S1, and the amplitudes of the displacement time histories remain within a range of 0.3 m. On the other hand, site S2 has three different azimuthal angles for the four hypocenter locations. Thus, if the azimuthal angle of a site remains about the same for different hypocenters, only small fluctuations arise in the ground motions, while large fluctuations can occur if the azimuthal angle of a site changes significantly. Moving the hypocenter from the

end of the fault to the center (HA to HD) has the same effect on the maximum velocities as cutting the length of the fault in half, e.g., the maximum horizontal velocity decreases 13% from the unilateral rupture to the symmetric bilateral rupture. This closely agrees with the 13% reduction in the maximum fault normal velocity observed by Inoue and Miyatake (1998) for a 50% decrease in the fault length.

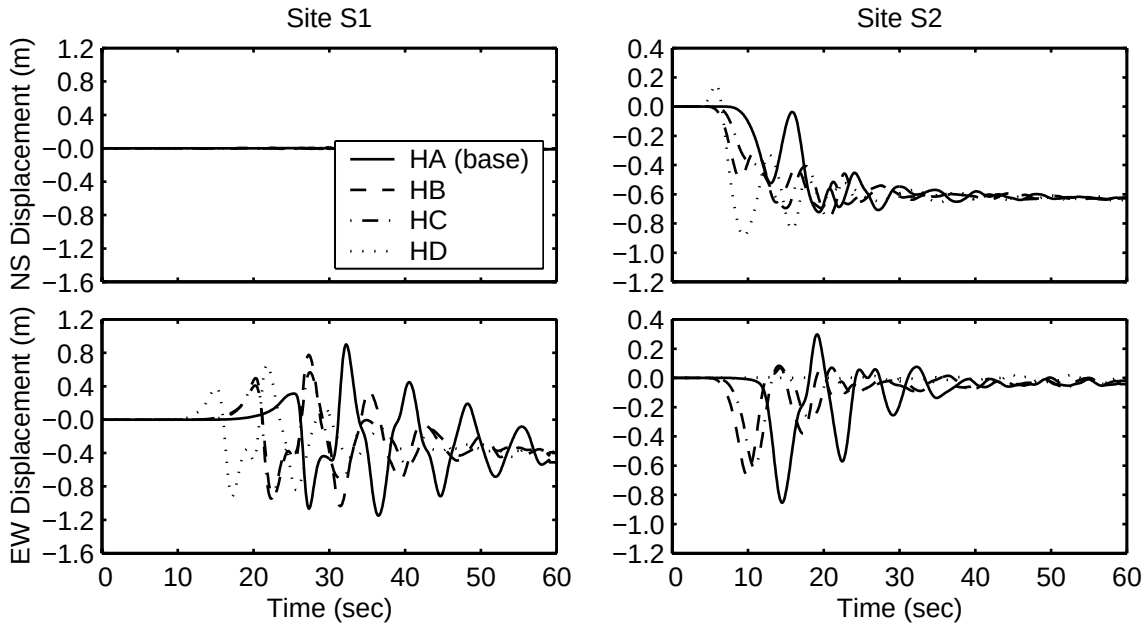

Figure 11. Comparison of horizontal displacement time histories at sites S1 and S2 for the four hypocenter locations.

The simulations include a homogeneous slip distribution in scenario base, a weakly heterogeneous slip distribution with a bias towards slip near the surface in scenario sliptop, a weakly heterogeneous slip distribution with a bias towards slip at depth in scenario slipbot, and a strongly heterogeneous slip distribution in scenario sliphet. Adding a small amount of heterogeneity results in almost no change in the displacement and velocity time histories at both sites S1 and S2 (Figure 12). At site S2 the strongly heterogeneous slip distribution causes moderate changes to the amplitudes and alters the shape of the displacement time histories. At site S1 energy from all points on the fault arrives closer together in time which greatly reduces the effect caused by the variation in the reinforcement of the shear wave from the heterogeneity. Therefore, the strongly heterogeneous slip distribution has much less of an effect at site S1 than it does at site S2. Coincidentally, at both sites the peak horizontal displacements and velocities remain relatively unchanged across all of the slip distribution scenarios (see Table 2). Based on the maximum displacements over the entire ground surface (see Aagaard 1999), we know that large perturbations in the slip distribution significantly alter the peak displacements at some locations very close to the fault. Additionally, including the high frequency portion of the ground motions would greatly increase the sensitivity of the motions (in the short period range) to heterogeneity in the final slip.

Increasing the average slip from 2.0 m in scenario base to 3.0 m in scenario slip3, while maintaining a peak slip rate of 1.5 m/sec, increases the amplitudes of the displacements but has little effect on the amplitudes of the velocities. This change in the average slip raises the moment magnitude of the earthquake from 7.0 to 7.1. The peak displacements do not increase

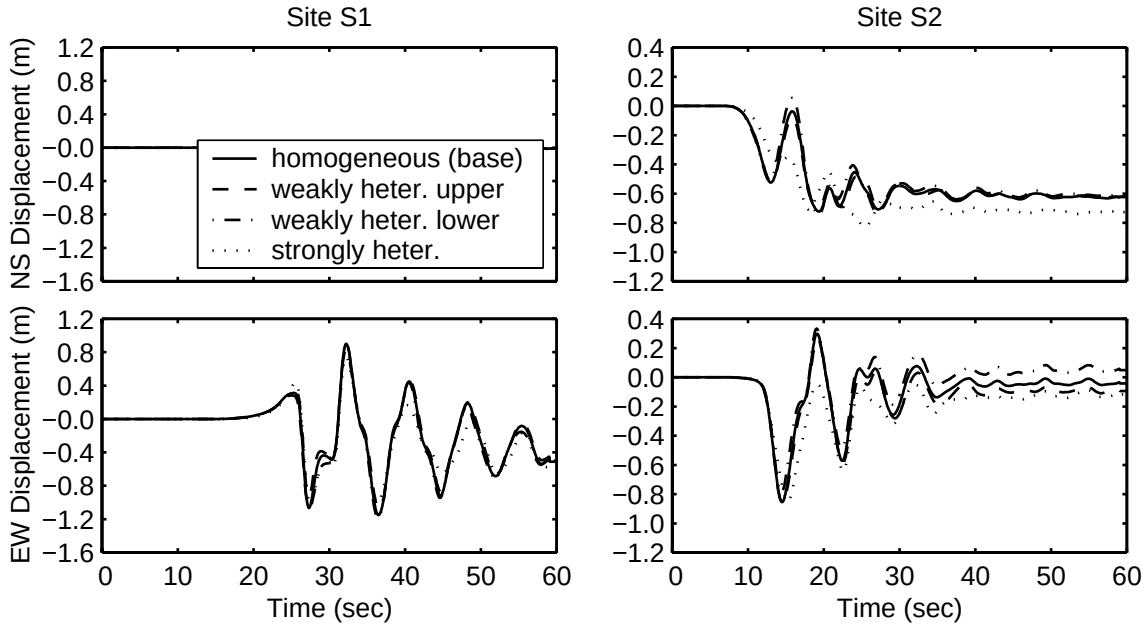

Figure 12. Comparison of horizontal displacement time histories at sites S1 and S2 for the four slip distributions.

as much as the average slip because the dynamic displacements exhibit a stronger sensitivity to the peak slip rate than the final slip. As a result of the 50% increase in the average slip, the peak displacements at sites site S1 and S2 increase by 17% and 33%, respectively.

We evaluate the effect of the depth of the fault using the results from scenarios base, fault4km, and fault8km. Increasing the depth of the top of fault, while using nearly identical slip distributions, shifts the slip to a region with a larger shear modulus and leads to a slight increase in the moment magnitude of the earthquake (see Heaton and Heaton 1989 for a detailed discussion of how changes in the material properties affect the moment magnitude). While dropping the fault has the same effect on the moment magnitude as increasing the average slip, the effect on the ground motions is very different. In general, the lower the depth of the fault, the smaller the amplitude of the ground motions at the surface. As the depth of the top of the fault increases, less slip occurs in the softer material at the top of the domain, and less energy refracts towards the ground surface. No slip occurs in the region of softer material when the top of the fault sits 8.0 km below the ground surface. This explains why dropping the fault to depths of 4.0 km and 8.0 km greatly reduces the amplitude of the displacements and velocities; the overall maximum horizontal displacements and velocities on the ground surface decrease by 45% and 41% for scenario fault4km and by 57% and 66% for fault8km relative to the case of surface rupture. Figure 13 illustrates this trend with the velocity time histories at sites S1 and S2. Inoue and Miyatake (1998) observed similar changes in the ground motions as they changed the fault depth in their dynamic ruptures, but they found a very large increase in the maximum velocities as the top of the fault approached the ground surface; the maximum fault normal velocities jumped from 1.1 m/sec to 3.8 m/sec for a 20 km long fault raised from a depth of 1.0 km to the free surface.

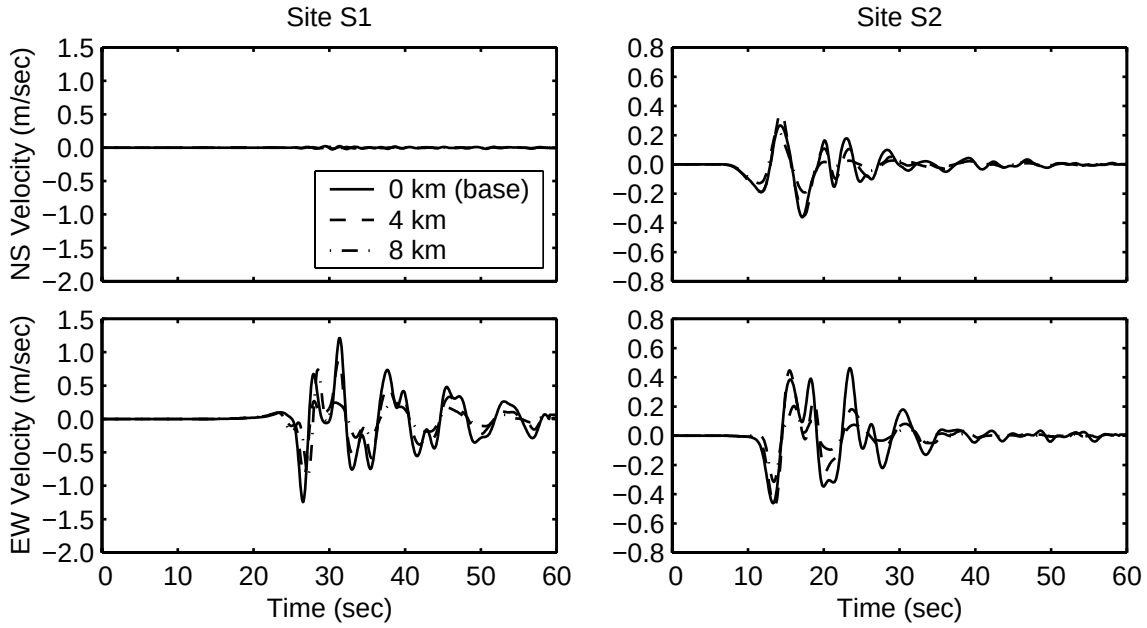

Figure 13. Comparison of horizontal velocity time histories at sites S1 and S2 for the three depths of the top of the fault.

THRUST FAULT

The geometry of the thrust fault closely resembles that of the Elysian Park fault underneath Los Angeles as described by Hall et al. (1995). The fault dips 23° to the north and measures 28 km long and 18 km wide. For most of the simulations, the top of the fault lies 8.0 km below the ground surface. The fault sits in a domain 60 km long by 60 km wide by 24 km deep as illustrated in Figure 14. We impose oblique slip with a rake angle of 105° from the strike to the west; this creates slip in the south-southeast direction. We use three finite-element models, one for each of the three fault depths. We follow the same procedure as in the strike-slip case: we globally refine the coarse meshes to the appropriate resolution for propagation of waves with periods down to 2.0 sec. After refinement, each mesh contains approximately 7.9 million elements and 5.1 million degrees of freedom. Each simulation took 1.2 hours using 256 processors of the Intel Paragon at the CACR.

Earthquake Source Parameters for the Thrust Fault

As in the strike-slip case, we systematically vary six earthquake source parameters: rupture speed, peak slip rate, hypocenter location, distribution of slip, average slip, and fault depth. Table 3 summarizes the parameters for each of the 14 simulations. The base case features a fault buried 8.0 km below the ground surface, a homogeneous slip distribution with an average slip of 1.0 m that is tapered at the edges, a rupture speed of 80% of the local shear-wave speed, a peak slip rate of 1.5 m/sec, and a hypocenter located at the bottom center of the fault (hypocenter HA). With the top of the fault 8.0 km below the ground surface and an average final slip of 1.0 m, the earthquakes have a moment magnitude of 6.8.

The four hypocenters (labeled HA through HD in Figure 14) lie along either the fault centerline or the east edge and either along the bottom edge or 4.0 km shallower. When the top of the fault lies 8.0 km below the ground surface, the bottom of the fault sits 15.0 km below the ground surface. We set the peak slip rate to either 1.0 m/sec, 1.5 m/sec, or 2.0 m/sec and

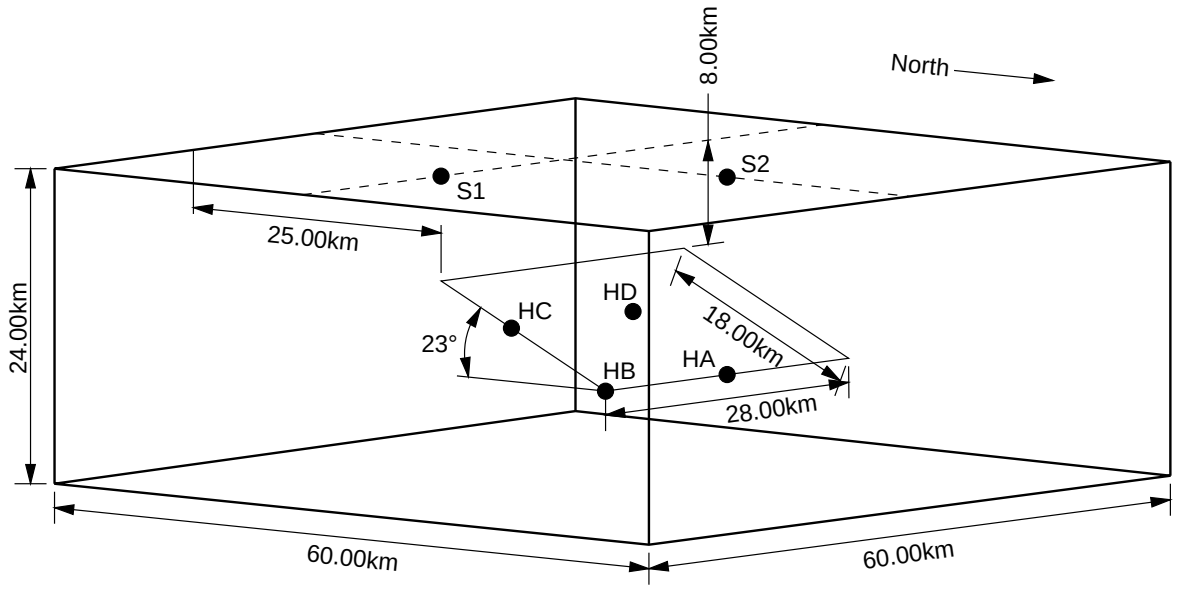

Figure 14. Domain geometry for the thrust fault for the case where the top of the fault lies 8.0 km below the ground surface. The labels HA through HD denote the various hypocenter locations. Waveforms are examined at site S1, which sits above the southeast corner of the fault, and site S2, which sits above hypocenter HA.

Table 3. Summary of the parameters for the simulations on the thrust fault

Scenario	Slip Pattern	Rup. Speed % of β	Peak Slip Rate (m/sec)	Hypo. Location	Fault Depth (km)	Avg. Slip (m)	Mom. Mag.
base	homogeneous	80	1.5	HA	8–15	1.0	6.8
vr70	homogeneous	70	1.5	HA	8–15	1.0	6.8
vr90	homogeneous	90	1.5	HA	8–15	1.0	6.8
vs10	homogeneous	80	1.0	HA	8–15	1.0	6.8
vs20	homogeneous	80	2.0	HA	8–15	1.0	6.8
hyB	homogeneous	80	1.5	HB	8–15	1.0	6.8
hyC	homogeneous	80	1.5	HC	8–15	1.0	6.8
hyD	homogeneous	80	1.5	HD	8–15	1.0	6.8
sliptop	weakupper	80	1.5	HA	8–15	1.0	6.8
slipbot	weaklower	80	1.5	HA	8–15	1.0	6.8
sliphet	strongheter	80	1.5	HA	8–15	1.0	6.8
slip2	homogeneous	80	1.5	HA	8–15	1.0	7.0
fault4km	homogeneous	80	1.5	HA	4–11	1.0	6.7
fault0km	homogeneous	80	1.5	HA	0–7	1.0	6.6

the rupture speed to either 70%, 80%, or 90% of the local shear-wave speed. The spatial distributions of final slip include homogeneous distributions that are tapered on all four edges, two weakly heterogeneous distributions (weakupper with a bias towards slip on the upper half of the fault plane and weaklower with a bias towards slip on the lower half of the fault plane), and a strongly heterogeneous distribution (strongheter shown in Figure 15). The heterogeneous slip distributions contain 20 asperities with uniform random distributions of radii, heights, and

locations. For the weakly heterogeneous distributions the asperity heights range from -0.25 m to 0.5 m with radii between 5.0 km and 8.0 km. Likewise, for the strongly heterogeneous distribution the asperity heights range from 0.0 m to 1.6 m with radii between 3.0 km and 6.4 km. In order to be able to study the sensitivity of the ground motions to the fault depth, we place the top of the fault at depths of 8.0 km, 4.0 km, and 0.0 km while maintaining the same length, width, and dip angle. Following the same procedure that we used to study the strike-slip simulations, we examine the base case in detail and analyze the other simulations in groups based on the variation of one of the parameters.

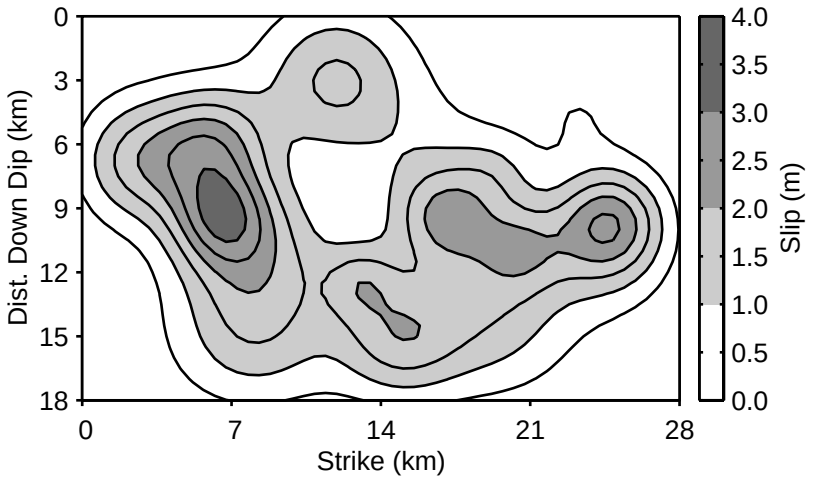

Figure 15. Strongly heterogeneous slip distribution strongheter which is tapered on all four edges with an average slip of 1.0 m and a maximum slip of 3.4 m.

Thrust Fault Base Case

Figure 16 displays the magnitude of the velocity vectors on the ground surface beginning at 6.0 sec for the base case. The seismic waves reach the ground surface approximately 5 sec after the rupture begins. A Rayleigh wave, which develops from the dilatational and shear waves hitting the free surface, causes the most severe motion in the 20 km wide region extending south from the surface projection of the top edge of the fault. The snapshot of the velocity at 10.0 sec clearly shows the Rayleigh wave as a double velocity pulse with peaks in both the positive and negative radial directions exceeding 0.8 m/sec. The maximum velocities develop in the second pulse at around 12 sec, after which the amplitudes decay because the Rayleigh wave receives no additional reinforcement from seismic waves propagating towards the surface from depth. The amplitude also decreases due to geometric spreading as the wave continues to propagate to the south.

The maximum horizontal displacements and velocities (Figure 17) occur five kilometers south of the top of the fault. The slip direction with a rake angle of 105° skews the maximum displacements and maximum velocities slightly towards the east. As the Rayleigh wave develops, the particle motion becomes more horizontal. This leads to a maximum horizontal displacement at the surface that is 1.5 times the maximum vertical displacement (1.1 m versus 0.75 m). The velocities exhibit an even greater disparity with the maximum horizontal velocity 3.0 times the maximum vertical velocity (1.2 m/sec versus 0.40 m/sec). The maximum horizontal velocities exceed 1.0 m/sec over an area of 61 km^2.

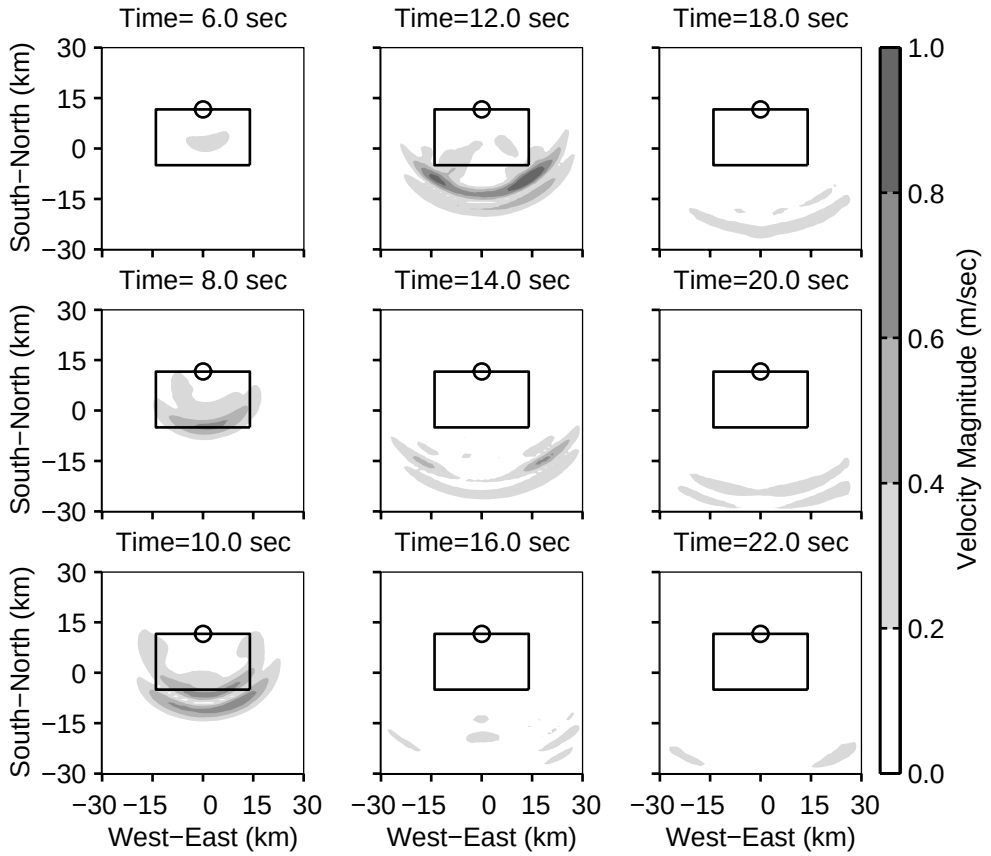

Figure 16. Snapshots of the magnitude of the velocity vector (0.5 Hz low-pass filtered) at each point on the ground surface for scenario base. The solid line indicates the projection of the fault onto the ground surface, and the hollow circle identifies the epicenter. The south-southeast slip direction (rake angle of 105°) creates the asymmetry in the east-west direction.

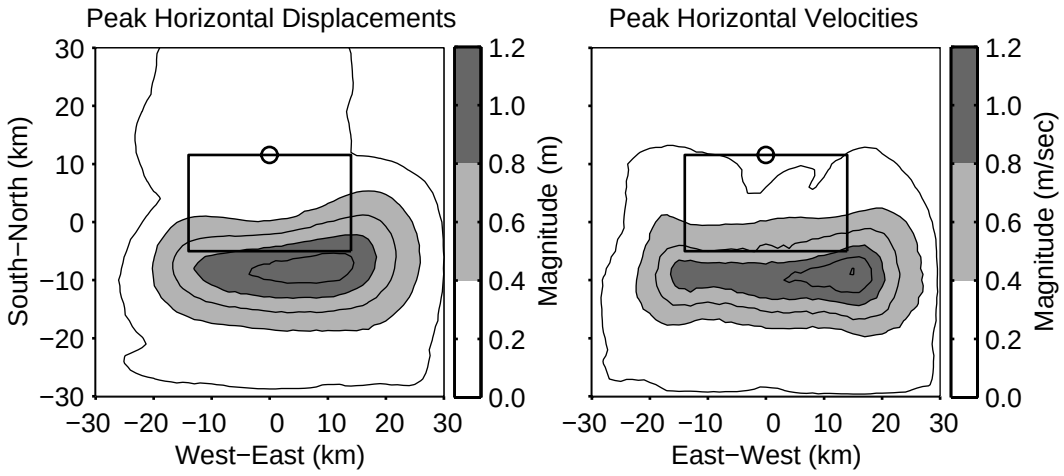

Figure 17. Maximum magnitudes of the horizontal displacement and velocity vectors (0.5 Hz low-pass filtered) at each point on the ground surface for scenario base. The solid line indicates the projection of the fault plane onto the ground surface, and the hollow circle identifies the epicenter. The south-southeast slip direction (rake angle of 105°) creates the asymmetry in the east-west direction.

The displacements and velocities at sites S1 and S2 given in Figure 18 exemplify the disparity between the motion in the forward direction (south of the fault) and the motion in the backwards direction (north of the fault). As shown in Figure 14, site S1 lies above the southeast corner of the fault, and site S2 lies above the center of the northern (bottom) edge of the fault, which in this case coincides with the epicenter. At site S1 the Rayleigh wave arrival consisting of a single pulse in displacement and a corresponding double pulse in velocity dominates the motion on all three components. The horizontal motion occurs almost exclusively in the southeast direction and is skewed to the east of the slip direction. Site S2 receives far less energy from the seismic waves.

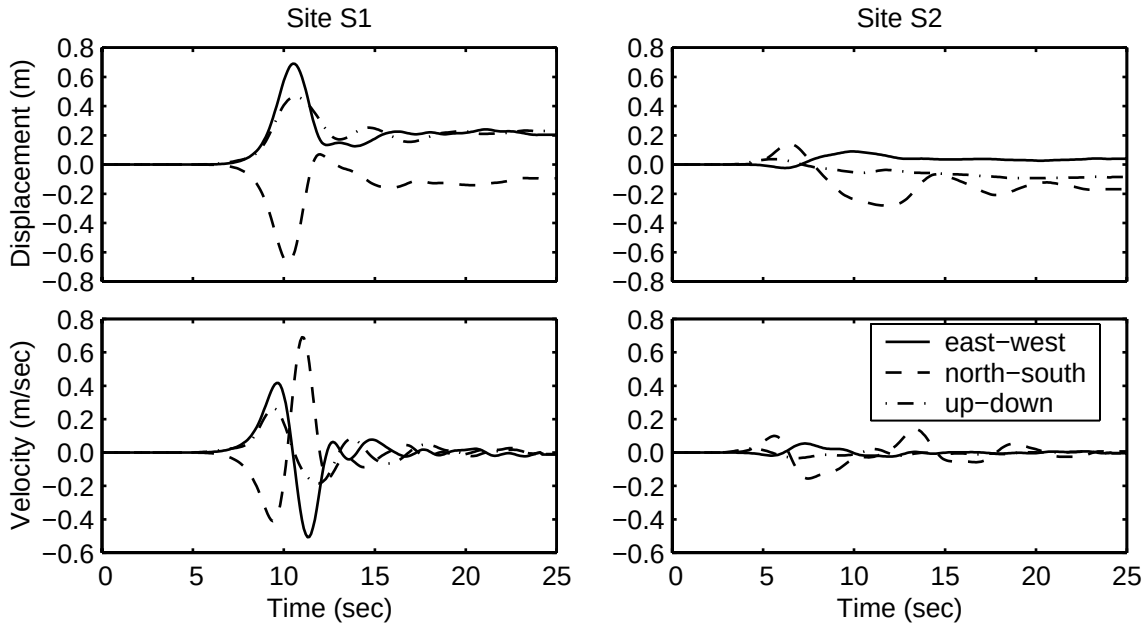

Figure 18. Displacement and velocity time histories at sites S1 and S2 for scenario base. Site S1 lies above the southeast corner of the fault, and site S2 lies at the epicenter.

We compute the response spectra at both sites following the same procedure used for the strike-slip fault. In this case, maximizing the peak-to-peak velocity requires rotating the ground motions at sites S1 and S2 to 140° and 170° east of north, respectively. The horizontal acceleration response spectra shown in Figure 19 illustrate the severity of the ground motion at site S1 (peak filtered acceleration of 0.15 g) compared to the rather benign motion at site S2. The response spectrum for site S1 displays a broad peak of 40% g centered around a period 2.6 sec. The response spectrum for site S2, in contrast, is nearly flat with a level below 5% g. Figure 19 also displays the *UBC* design spectrum for a site with soil class S_D in zone 4 that lies within 2 km of a fault designated as source type *B*. The site S1 spectrum falls well below the *UBC* spectrum for periods greater than 5 sec and just slightly above for periods between 2.5 sec and 4 sec.

Summary of Results for the Thrust Fault

We again summarize the general variability in the ground motions by tabulating the overall maximum horizontal displacements and velocities on the ground surface and at sites S1 and S2 for each scenario as shown in Table 4. We will refer to these values in our discussion of how the parameters affect the ground motions.

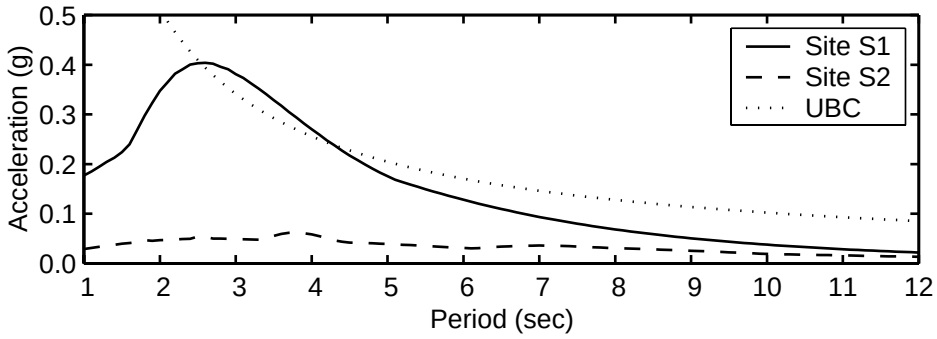

Figure 19. Horizontal acceleration response spectra for 5% critical damping at sites S1 and S2 for scenario base. The ground motions have been low-pass filtered to include periods greater than 2.0 sec. The dotted line indicates the *UBC* design spectrum for a site with soil class S_D in zone 4 that lies within 2 km of a fault designated as source type *B*.

Table 4. Maximum displacements and velocities (0.5 Hz low-pass filtered) at site S1, site S2, and on the ground surface for each thrust fault scenario

Scenario	Mom. Mag.	Avg. Slip (m)	Max. Horiz. Disp.			Max. Horiz. Vel.		
			S1 (m)	S2 (m)	surface (m)	S1 (m/sec)	S2 (m/sec)	surface (m/sec)
base	6.8	1.0	0.95	0.29	1.1	0.83	0.16	1.2
vr70	6.8	1.0	0.76	0.27	0.86	0.55	0.11	0.91
vr90	6.8	1.0	1.1	0.31	1.4	1.1	0.22	1.7
vs10	6.8	1.0	0.86	0.29	0.99	0.64	0.14	0.95
vs20	6.8	1.0	0.99	0.29	1.2	0.92	0.18	1.4
hyB	6.8	1.0	0.44	0.27	0.78	0.26	0.14	0.77
hyC	6.8	1.0	0.30	0.31	0.58	0.16	0.21	0.55
hyD	6.8	1.0	0.76	0.35	0.80	0.51	0.23	0.64
sliptop	6.8	1.0	0.83	0.37	1.1	0.61	0.18	1.2
slipbot	6.8	1.0	0.96	0.29	1.1	0.91	0.17	1.2
sliphet	6.8	1.0	1.0	0.30	1.1	0.94	0.20	1.3
slip2	7.0	2.0	1.6	0.57	1.8	0.99	0.24	1.4
fault4km	6.7	1.0	1.3	0.38	1.6	1.4	0.24	1.8
fault0km	6.6	1.0	1.0	0.94	1.3	1.1	1.1	1.5

We study the sensitivity of the ground motions to the rupture speed using scenarios vr70, base, and vr90 with rupture speeds of 70%, 80%, and 90% of the local shear-wave speed, respectively. A faster rupture speed increases the maximum horizontal velocities at site S1 from 0.55 m/sec to 0.83 m/sec to 1.1 m/sec and at site S2 from 0.11 m/sec to 0.16 m/sec to 0.22 m/sec. The vertical components show no corresponding increase. Increasing the rupture speed causes the waves from all portions of the fault to arrive in a shorter time interval which leads to sharper phase arrivals. As a result, the width of the double pulse in velocity at site S1 decreases as the rupture speed increases.

Scenarios vs10, base, and vs20 with peak slip rates of 1.0 m/sec, 1.5 m/sec, and 2.0 m/sec, respectively, illustrate the sensitivity of the ground motions to changes in the peak slip rate. Figure 20 demonstrates that the peak slip rate influences the amplitude of motion but not the shape

of the waveforms. Increasing the peak slip rate from 1.0 m/sec to 1.5 m/sec causes the overall maximum velocity on the ground surface to increase from 0.95 m/sec to 1.2 m/sec, while increasing it another 0.50 m/sec causes the peak velocity to increase an additional 0.2 m/sec.

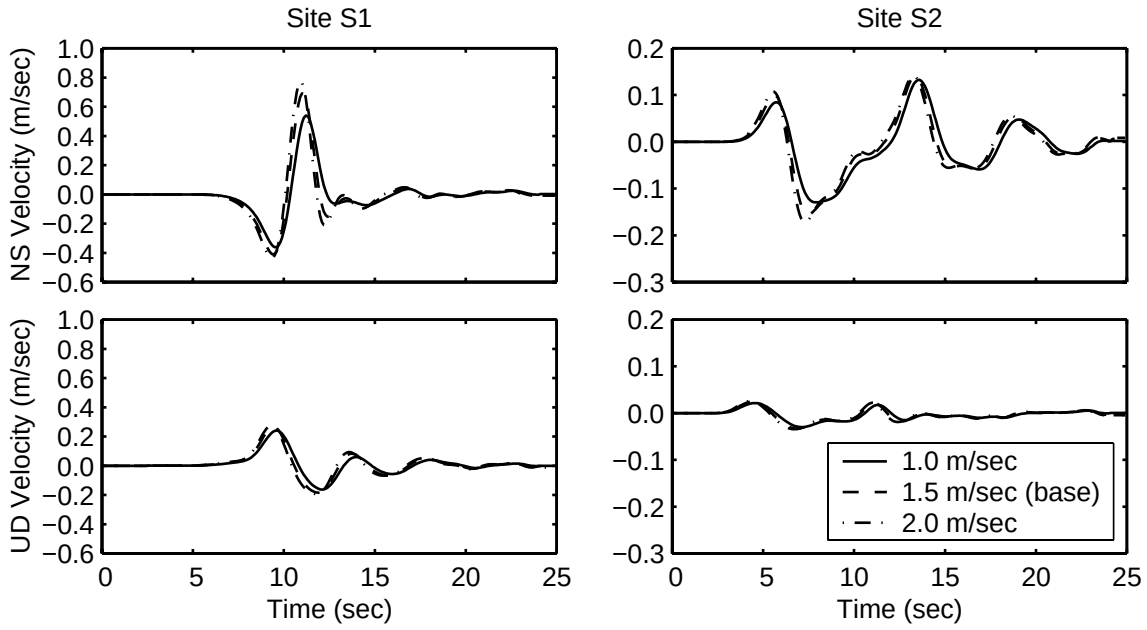

Figure 20. Comparison of north-south and vertical velocity time histories at sites S1 and S2 for the three peak slip rates.

We examine the variability of the ground motions to changes in the location of the hypocenter using scenario base, scenario hyB, scenario hyC, and scenario hyD. In general, the displacement amplitudes increase the greater the distance the fault ruptures toward the site and for sites with azimuthal angles close to zero degrees. Site S1 has a different azimuthal angle for each hypocenter location, while site S2 has three different azimuthal angles for the four hypocenter locations. As expected from the observations of the ground motions from the strike-slip fault, at both sites S1 and S2 the displacement time histories for the different hypocenter locations differ considerably when the sites have substantially different azimuthal angles. For example, at site S1 moving the hypocenter from HD to HA increases the distance the rupture propagates towards the site and places site S1 closer to an azimuthal angle of zero degrees. As a result, the peak horizontal displacement increases by 25% (from 0.76 m to 0.95 m) (see Figure 21). Placing the hypocenter along the east edge of the fault limits the directivity of the rupture towards site S1 by reducing the area on the fault where the direction of the rupture propagation roughly matches the slip direction. As a result, shifting the hypocenter from HA to HB reduces the peak displacement at site S1 by 54%.

The simulations use a homogeneous slip distribution in scenario base, a weakly heterogeneous slip distribution with a bias towards slip on the upper half of the fault plane in scenario sliptop, a weakly heterogeneous slip distribution with a bias towards slip on the lower half of the fault plane in scenario slipbot, and a strongly heterogeneous slip distribution in scenario sliphet. The locations of the asperities shift the distribution of the maximum displacements and velocities on the ground surface, but the overall maximum horizontal displacements and velocities differ by less than 0.04 m and 0.07 m/sec, respectively. At site S1 we find small variations in the amplitude of the displacement pulse associated with the Rayleigh wave arrival

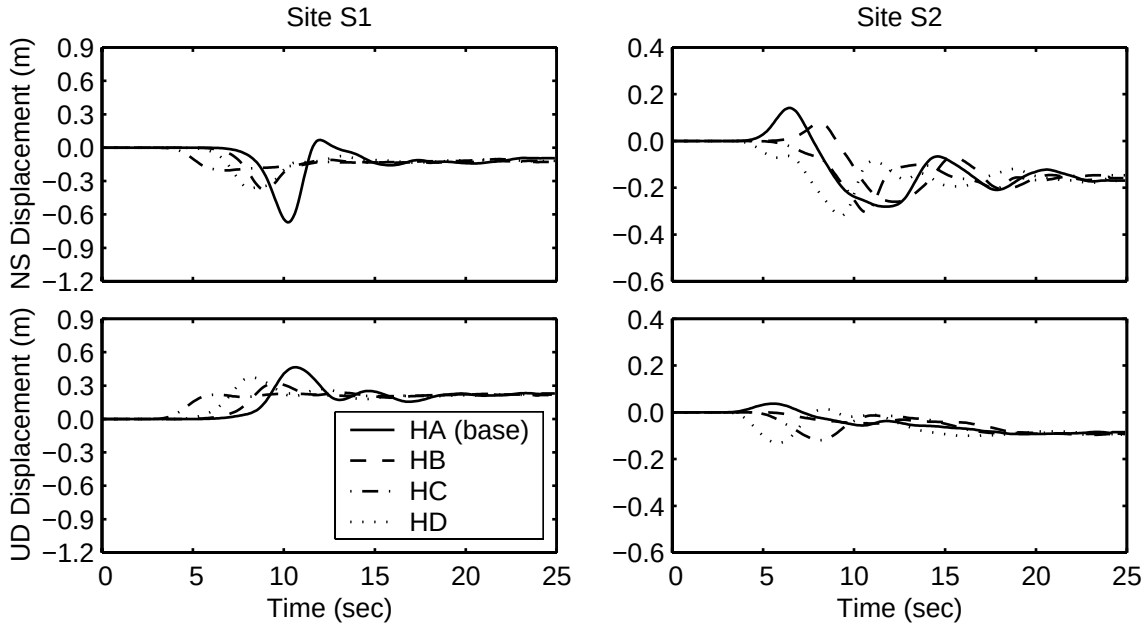

Figure 21. Comparison of north-south and vertical displacement time histories at sites S1 and S2 for the four hypocenter locations.

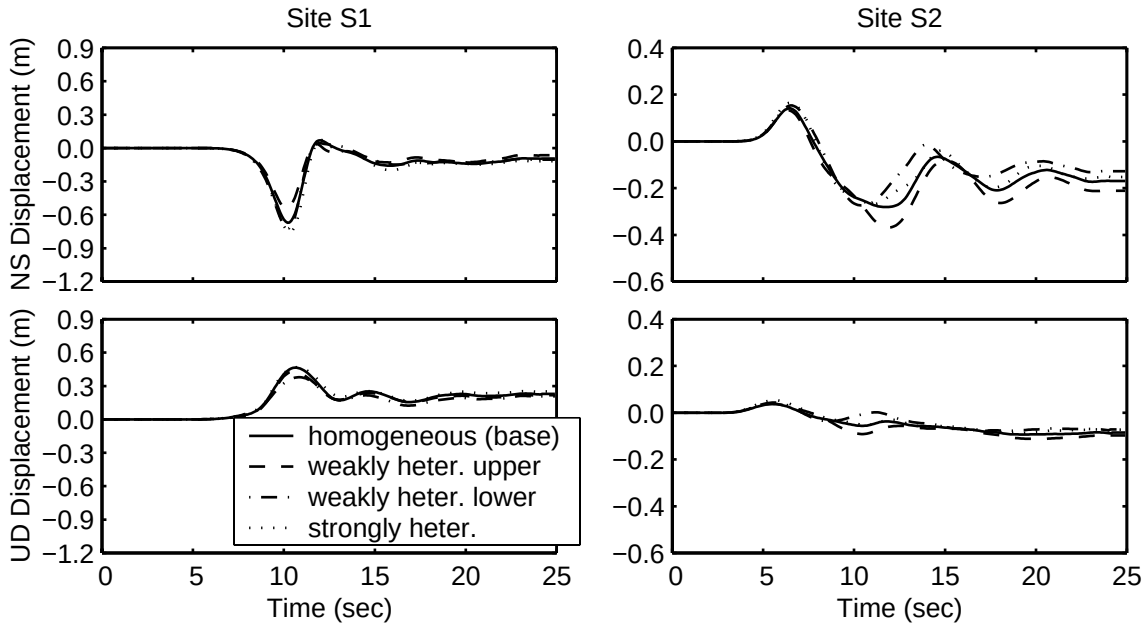

Figure 22. Comparison of north-south and vertical displacement time histories at sites S1 and S2 for the four slip distributions.

with peak horizontal displacements of 0.95 m for scenario base, 0.83 m for scenario sliptop, 0.96 m for scenario slipbot, and 1.0 m for scenario sliphet. However, as shown in Figure 22, the remainder of the displacement time histories appear unaffected by the heterogeneity in the slip distributions. At site S2 the ground motion displays no noticeable variation until nearly 10 sec, after which the ground motion in the north-south direction remains noticeably different for the remainder of the records.

Increasing the average slip from 1.0 m in scenario base to 2.0 m in scenario slip2, while maintaining the same peak slip rate, causes a large increase in the displacement amplitudes, but only a small increase in the velocity amplitudes. The overall maximum horizontal displacement on the ground surface jumps from 1.1 m to 1.8 m, while the maximum horizontal velocity displays a small increase from 1.2 m/sec to 1.4 m/sec. This doubling of the average slip changes the moment magnitude from 6.8 to 7.0. Varying the average slip affects both the north-south and vertical displacement components at sites S1 and S2 as illustrated in Figure 23.

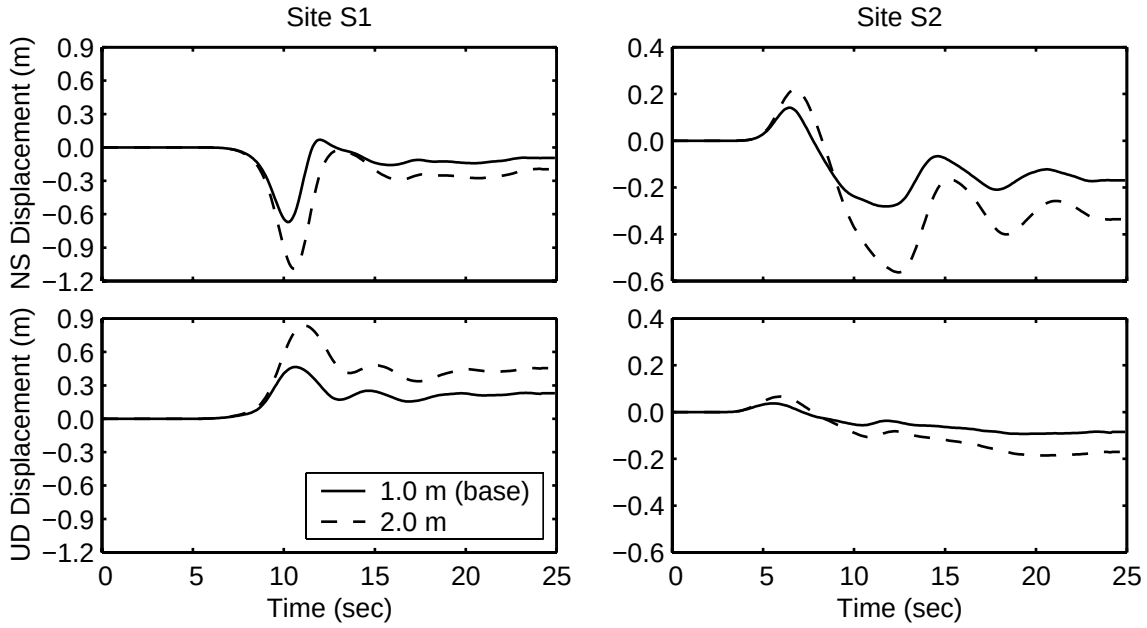

Figure 23. Comparison of north-south and vertical displacement time histories at sites S1 and S2 for the two values of average slip.

We study the effect that changing the depth of the fault has on the ground motions using scenario base, where the top of fault sits at a depth of 8.0 km, and scenarios fault4km and fault0km. Raising the top of the fault so that slip occurs in softer material reduces the moment magnitude from 6.8 (8.0 km depth) to 6.7 (4.0 km depth) and 6.6 (0.0 km depth). While the moment magnitude decreases, the ground motions become much more severe, particularly directly above the top of the fault. As the slip shifts closer to the ground surface, the displacements on the hanging wall (above the fault) increase more than the displacements on the footwall (below the fault). Raising the top of the fault to a depth of 4.0 km increases the overall maximum horizontal velocity by 50%, and the area subjected to a maximum velocity exceeding 1.0 m/sec jumps from 61 km^2 to more than 260 km^2. Furthermore, with the top of the fault at the ground surface, the rupture generates additional large amplitude surface waves. These results are consistent with those of Mikumo and Miyatake (1993) who found the near-source ground motions very sensitive to the depth of the fault.

Figure 24 displays the maximum horizontal displacements and velocities on the ground surface along the north-south centerline for the three fault depths. When we raise the top of the fault to the ground surface, the maximum displacements directly above the fault exhibit a greater increase than those up-dip from the fault. The multiple peaks for this scenario (fault0km) come from the complex interaction of the waves generated at various locations over the fault. This interaction exhibits a strong sensitivity to conditions on the fault.

Prescribed ruptures, such as the ones used in this study, have transparent fault conditions which allow normally incident shear waves to propagate through the fault as if it did not exist. On the other hand, dynamic ruptures have nontransparent fault conditions that predominantly reflect normally incident shear waves attempting to propagate through the slipping portion of the fault. As a result, in dynamic (self-slipping) ruptures the slipping section of the fault can reflect shear waves, thereby trapping energy on the hanging wall (north) side of the fault; the displacements and velocities are then much smaller on the footwall (south) side of the fault (Mikumo and Miyatake 1993, Brune 1996, Oglesby et al. 1998, Shi et al. 1998, Oglesby et al. 2000a, Oglesby et al. 2000b, Aagaard et al.). For the base case with a fault depth of 8.0 km, the curve for the maximum displacements and the curve for the maximum velocities peak 5.0 km south of the surface projection of the top edge of the fault. When the top of the fault sits 4.0 km below the surface, the maximum displacements and velocities contain two peaks, each associated with the maximum amplitude of a different Rayleigh wave.

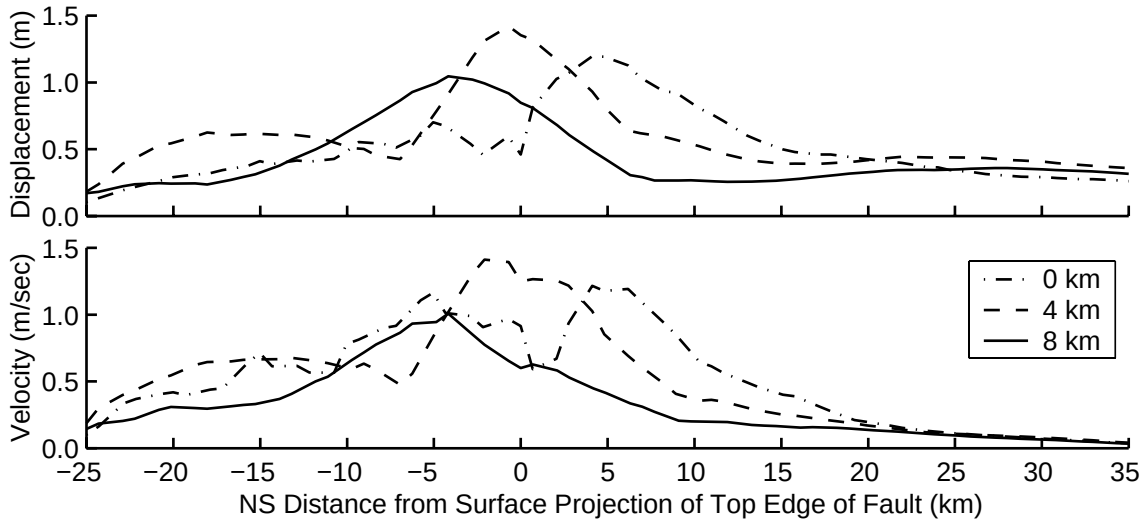

Figure 24. Maximum magnitudes of the horizontal displacement vectors and velocity vectors along a north-south line running over the center of the fault for the three depths of the fault.

DISCUSSION

The earthquake simulations on the strike-slip fault share several distinct characteristics. Directivity causes the peak displacements to increase along the strike of the fault away from the epicenter until the end of the fault where they decay rapidly with distance. A typical ground motion contains a large-amplitude shear wave followed by a train of surface waves with progressively smaller amplitudes. The most severe component of ground motion occurs in the direction normal to the fault. We also find several common features for the simulations where the top of the thrust fault lies 8.0 km below the ground surface. The shallow dip of the fault to the north causes the maximum displacements and velocities to occur approximately 5 km south of the surface projection of the top edge of the fault for up-dip rupture. The rake angle of 105° directs the largest displacements and velocities towards the southeast. A large, single pulse in displacement and a corresponding large, double pulse in velocity associated with a Rayleigh wave characterize the ground motions towards the south (the forward direction). The ground motions towards the north (the backward direction) are much smaller. All of these features come from the directivity of the rupture.

Based upon the changes of the ground motions in response to the systematic variation of the seismic source parameters, we characterize the sensitivity of the ground motions to each of the source parameters. Raising the top of both the strike-slip fault and the thrust fault causes the ground motions to become much more severe with large-amplitude surface waves. Consequently, the ground motions at all sites on the ground surface exhibit a strong sensitivity to the fault depth. As the rupture speed increases, the reinforcement of the shear wave in the strike-slip cases and the Rayleigh wave in the thrust fault cases becomes more efficient. This increases the amplitude of both the displacements and velocities while narrowing the pulse widths. Thus, the ground motions appear moderately sensitive to variations in the rupture speed. The ground motions also display moderate sensitivity to the changes in the peak slip rate. Increasing the peak slip rate directly increases the peak velocities and leads to larger displacement amplitudes. However, on both faults the phase arrivals remain relatively unchanged. Hence, the peak slip rate influences the amplitude of the motion but not the shapes of the waveforms.

Increasing the average slip results in a significant, but correspondingly smaller, relative increase in the peak displacements and little change in the peak velocities, because we maintain the same rupture speed and peak slip rate. At a given site the sensitivity of the ground motions to the location of the hypocenter depends on the relative change in the azimuthal angle. On both faults the ground motions exhibit little change when the azimuthal angle remains about the same for different hypocenter locations, but large variations in the ground motions occur when the azimuthal angle changes significantly with different hypocenters. In some cases the site may move off of or onto a nodal line, and the ground motions increase or decrease by very large amounts.

The ground motions exhibit little sensitivity to the addition of heterogeneity into the distribution of final slip, particularly in the forward direction. Graves (1998) also found near-source ground motions relatively insensitive to weakly heterogeneous slip distributions; however, he found large reductions in the peak velocities with a strongly heterogeneous distribution of slip. In contrast to our simulations, he lengthened the slip duration on the shallow portion of the fault based on the kinematic source model of the 1992 Landers earthquake from Wald and Heaton (1994). This significantly disrupts the efficiency of the reinforcement of the shear wave and surface waves by the rupture and leads to a decrease in the amplitude of the motion. As previously noted in the discussion of the choice of the slip rates and rupture speeds, considerable uncertainty still exists regarding the duration of slip for very shallow rupture, and lengthening of the duration of slip near the surface may or may not be realistic. However, we expect the high frequency portion of the ground motions, which we do not include in the simulations, to exhibit a greater sensitivity to heterogeneity in the final slip. Similarly, Spudich and Frazer (1984) found heterogeneity in either the distribution of slip or the rupture speed could account for variations in high frequency (> 1 Hz) ground velocities and accelerations.

In order to quantify the variability of the maximum horizontal displacements and velocities due to directivity, we consider identical events occurring independently and end to end along infinite extensions of our strike-slip fault and our thrust fault as illustrated in Figure 25 for the strike-slip fault. This creates periodic distributions of the maximum displacements and velocities. At each location on the ground surface, we select the greatest maximum horizontal displacement and velocity over all the earthquakes occurring along the infinitely long fault. We consider the effect of the depth of the fault using strike-slip scenarios base, fault4km, fault8km (all unilateral with hypocenter HA) and thrust fault scenarios base, fault4km, fault0km (all up-dip ruptures with hypocenter HA).

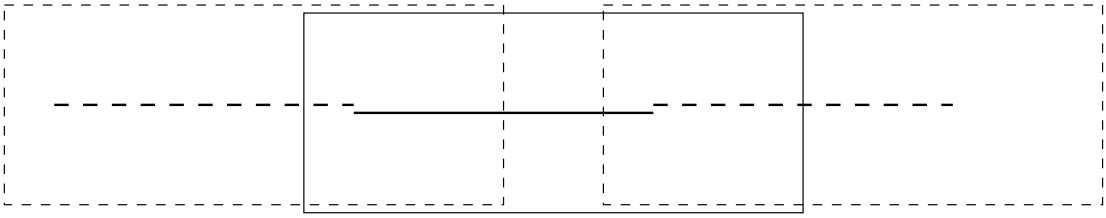

Figure 25. Diagram showing the construction of an infinitely long fault composed of identical strike-slip fault domains with the faults lying end to end. The solid lines identify the original domain, and the dashed lines identify domains (with a slight offset for clarity) added to each end to extend the fault. We compile distributions of the maximum displacement and velocity as a function of distance from the infinitely long fault by selecting the maximum values from the overlapping distributions of the displacements and velocities associated with each domain.

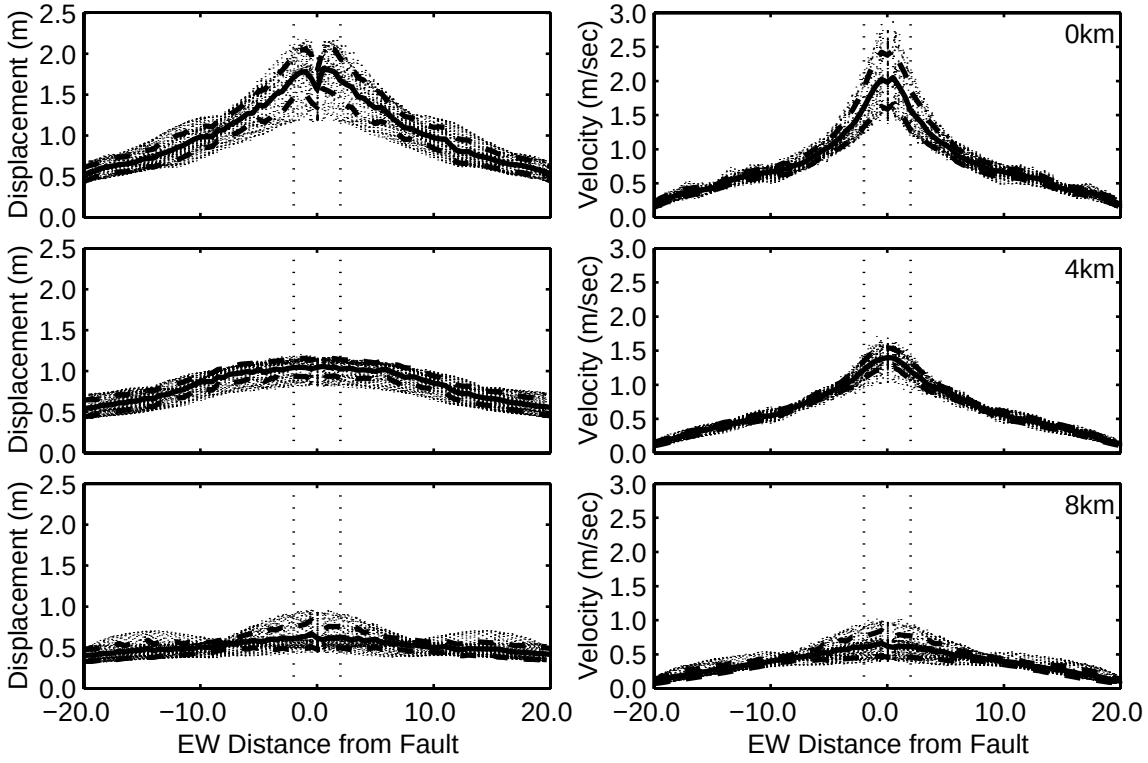

Figure 26. Maximum horizontal displacements and velocities on the ground surface as a function of distance from the surface projection of the top edge of the strike-slip fault for the three fault depths. The thick lines display the average and plus or minus one standard deviation. The vertical, dotted lines bound the zone with the highest near-source factor from the 1997 *UBC*.

Using these periodic distributions of shaking, we compile the maximum displacements and velocities as a function of distance from the top edge (or its surface projection) of the strike-slip fault and thrust fault as shown in Figures 26 and 27. The thick lines identify the mean and plus and minus one standard deviation of the distribution. Directivity causes substantial variability in the peak motions along the fault at any given distance from the top edge. For example, next to the fault in strike-slip scenario base, the maximum horizontal displacements range from 1.2 m to 1.9 m and the maximum horizontal velocities range from 1.4 m/sec to 2.8 m/sec. Similarly, 5.0 km up-dip from the projection of the top edge of the thrust fault, the maximum displacements range from 0.80 m to 1.0 m and the maximum velocities range

from 0.84 m/sec to 1.2 m/sec for thrust scenario base. Additionally, Figures 26 and 27 further illustrate the sensitivity of the ground motions to the depth of the fault.

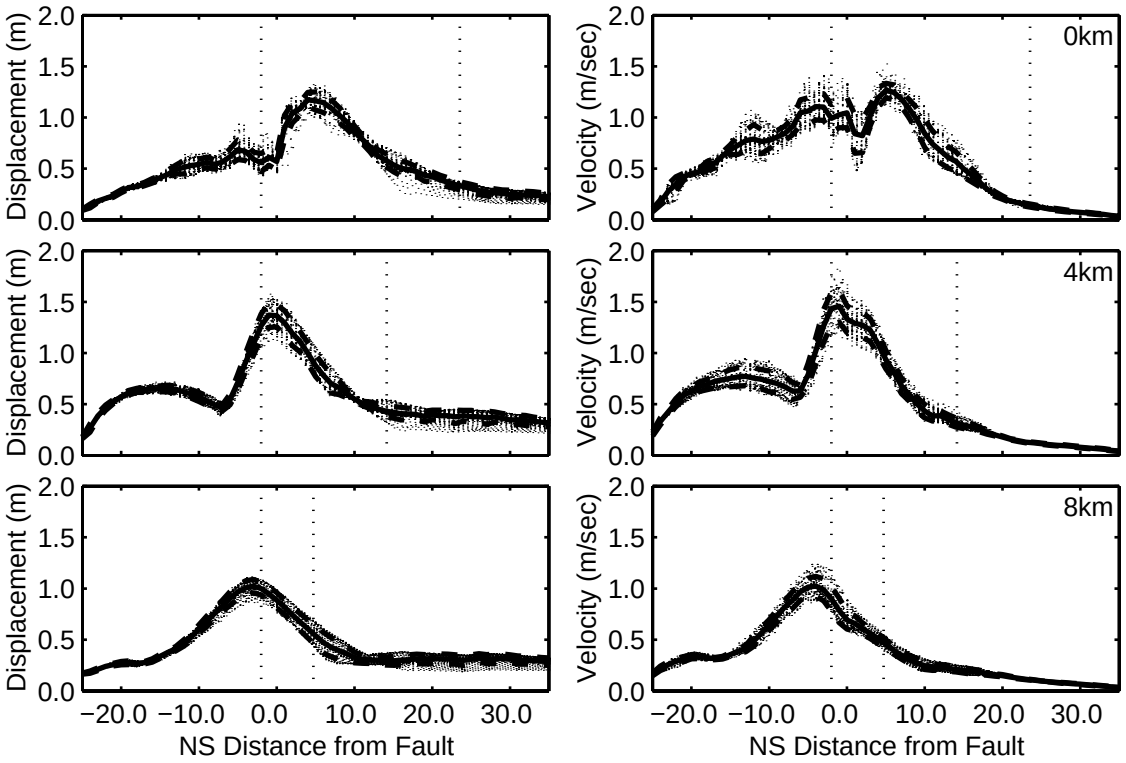

Figure 27. Maximum horizontal displacements and velocities on the ground surface as a function of distance from the surface projection of the top edge of the thrust fault for the three fault depths. The thick lines display the average and plus or minus one standard deviation. The vertical, dotted lines bound the zone with the highest near-source factor from the 1997 *UBC*.

If the maximum ground displacements and velocities correlate with the seismic demand on a building, then the region in which these peak motions occur should coincide with the zone with the highest near-source factor as defined by the 1997 *UBC* (see Hall 1998). In the *UBC* the zone with the highest near-source factor corresponds to the area within 2 km of the surface projection of the portion of the fault that lies above a depth of 10 km. In Figures 26 and 27 we identify the boundaries of this zone with the vertical lines. For the strike-slip cases, the zone with the highest near-source factor, although narrow, correctly matches the region subjected to the most severe motion. However, for the thrust fault cases, the region of the maximum displacements and velocities is skewed in the up-dip direction relative to the zone with the highest near-source factor. When the top of the fault lies 8 km below the ground surface, the peak ground motions occur 5 km up-dip from the surface projection of the top edge of the fault. Some correction for buried faults appears necessary. The extension of the zone with the highest near-source factor over the fault in the down-dip direction appears unnecessary, but may be justified by the presence of short-period ground motions which we do not include in the present simulations.

Finally, we compare the distributions of the ground motions on the surface for strike-slip fault scenario base and thrust fault scenario slip2. Figure 28 displays the area on the ground surface where the maximum horizontal displacements and velocities exceed a given value. The

areas where the maximum values exceed zero correspond to the total areas of the ground surfaces in the two domains. For the strike-slip fault, 1300 km^2 of the ground surface experiences displacements of at least 1.0 m and 690 km^2 experience velocities greater than 1.0 m/sec. The corresponding values for the thrust fault are much smaller.

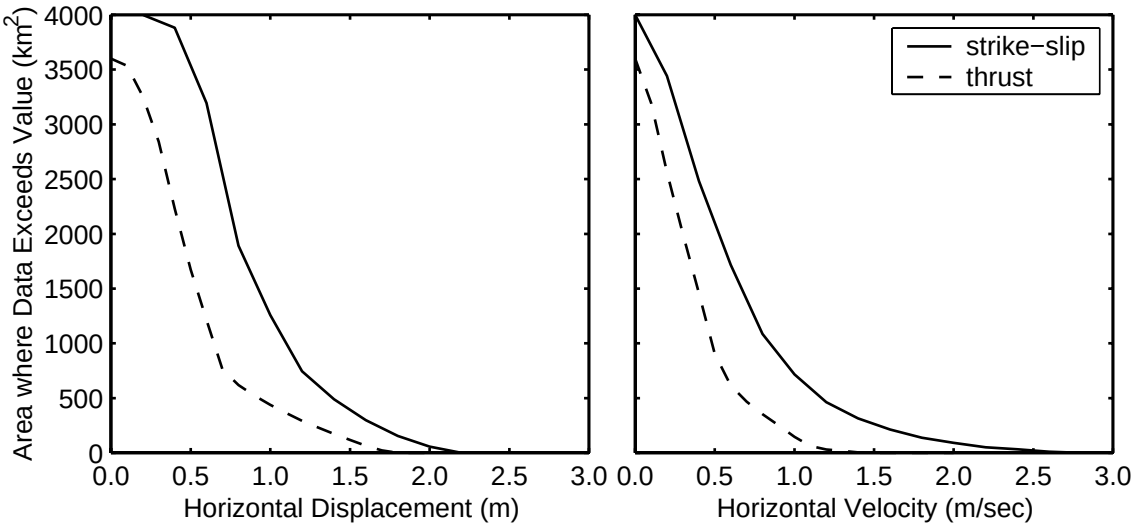

Figure 28. Areas on the ground surface in the strike-slip and thrust fault domains where the maximum horizontal displacements and velocities exceed a given value.

While both have an average slip of 2.0 m and a moment magnitude of 7.0, the rupture length of the strike-slip event is 2.1 times greater than that for thrust event, so we attribute the disparity between the curves in Figure 28 to the difference in the rupture lengths. The location of the top of the strike-slip fault at the surface compared to the top edge of the thrust fault at a depth of 8 km also contributes to the differences between the curves. For the thrust fault the shallow dip angle of 23° and the 28 km fault length lead to the velocity pulse sweeping across a large area, but the 18 km fault width limits the distance over which the rupture reinforces the Rayleigh wave. For the strike-slip fault the vertical dip of the fault tends to confine the velocity pulses to the region close to the fault, but the 60 km fault length allows the rupture to reinforce the shear wave over a much greater distance compared to the thrust fault. Thus, we find the greater fault length of the strike-slip fault has a greater impact than the shallow dip of the thrust fault, so that the area on the ground surface subjected to the near-source directivity effect is larger for the strike-slip fault than for the thrust fault.

CONCLUSIONS

This sensitivity study shows that in order to accurately model long-period near-source ground motions for engineering design, we must carefully select the values for those parameters that cause the most variability in the resulting motions. These parameters include the depth of the fault, the rupture speed, the peak slip rate, and the average slip. The most severe cases of ground motion will occur when the rupture propagates as far as possible towards the site under study and the site has an azimuthal angle close zero degrees. As long as the site sits in the forward direction, the spatial distribution of slip on the fault has a minor influence on the long-period ground motions, so we need not model it with as much care as the other source parameters.

Large displacement and velocity pulses dominate the ground motions in the forward direction. The dynamic displacements close to the fault are comparable to the average slip and decrease roughly by a factor of three over a 10 km distance from the fault. The areal extent subjected to strong near-source directivity effects from a strike-slip earthquake can be quite large and much greater than that from an earthquake of a similar magnitude on a buried thrust fault. However, for our M 6.8 thrust events with the top of the fault at a depth of 8.0 km, a double pulse in velocity still sweeps across a significant region with a peak velocity exceeding 1.0 m/sec over an area of 61 km^2. Consequently, near-source effects are important for buried thrust faults. For our 8.0 km deep buried case, the peak ground displacements and velocities occur 5 km up-dip from the surface projection of the top edge of the fault, which lies outside the zone of the highest near-source factor obtained from applying the 1997 *UBC* formulation.

ACKNOWLEDGMENTS

This work was supported by a National Science Foundation fellowship, the Southern California Earthquake Center, and the California Institute of Technology. We would like to thank Steve Day and two anonymous reviewers for their helpful comments. Access to the 512 Node Intel Paragon computer, located at the California Institute of Technology, was provided by the Center for Advanced Computing Research.

REFERENCES

Aagaard, B. T., 1999, Finite-element simulations of earthquakes, *Technical Report 99-03*, California Institute of Technology, Earthquake Engineering Research Laboratory, Pasadena, CA.

Aagaard, B. T., Heaton, T. H., and Hall, J. F., Dynamic earthquake ruptures in the presence of lithostatic normal stresses: Implications for friction models and heat production, *Bulletin of the Seismological Society of America*, in press.

Archuleta, R. J. and Frazier, G. A., 1978, Three-dimensional numerical simulations of dynamic faulting in a half-space, *Bulletin of the Seismological Society of America*, **68**(3), 541–572.

Bao, H. S., Bielak, J., Ghattas, O., Kallivokas, L. F., O'Hallaron, D. R., Shewchuk, J. R., and Xu, J. F., 1998, Large-scale simulation of elastic wave propagation in heterogeneous media on parallel computers, *Computer Methods in Applied Mechanics and Engineering*, **152**(1-2), 85–102.

Brune, J. N., 1970, Tectonic stress and spectra of seismic shear waves from earthquakes, *Journal of Geophysical Research*, **75**, 4997–5009.

Brune, J. N., 1996, Particle motion in a physical model of shallow angle thrust faulting, *Proceedings of the Indian Academy of Sciences: Earth and Planetary Sciences*, **105**(2), L197–L206.

Cohen, M., 1980, Silent boundary conditions for transient wave analysis, *Technical Report 80-09*, California Institute of Technology, Earthquake Engineering Research Laboratory, Pasadena, CA.

Day, S. M., 1982, Three-dimensional simulation of spontaneous rupture: The effect of nonuniform prestress, *Bulletin of the Seismological Society of America*, **72**(6), 1881–1902.

Freund, L., 1979, The mechanics of dynamic shear crack propagation, *Journal of Geophysical Research - Solid Earth*, **84**(B5), 2199–2209.

Fukuyama, E. and Madariaga, R., 2000, Dynamic propagation and interaction of a rupture front on a planar fault, *Pure and Applied Geophysics*, **157**(11-12), 1959–1979.

Graves, R. W., 1998, Three-dimensional finite-difference modeling of the San Andreas fault: Source parameterization and ground-motion levels, *Bulletin of the Seismological Society of America*, **88**(4), 881–897.

Hall, J., 1998, Seismic response of steel frame buildings to near- source ground motions, *Earthquake Engineering & Structural Dynamics*, **27**(12), 1445–1464.

Hall, J. F., Heaton, T. H., Halling, M. W., and Wald, D. J., 1995, Near-source ground motion and its effects on flexible buildings, *Earthquake Spectra*, **11**(4), 569–605.

Heaton, T. H., 1990, Evidence for and implications of self-healing pulses of slip in earthquake rupture, *Physics of the Earth and Planetary Interiors*, **64**(1), 1–20.

Heaton, T. H., 1995, Overview of seismological methods for the synthesis of strong ground motion, *Proceedings: Modeling Earthquake Ground Motion at Close Distances*, Research Project 3102-04, Electric Power Institute, Palo Alto, CA, 15-1 – 15-17.

Heaton, T. H., Hall, J. F., Wald, D. J., and Halling, M. W., 1995, Response of high-rise and base isolated buildings to a hypothetical Mw 7.0 blind thrust earthquake, *Science*, **267**(5195), 206–211.

Heaton, T. H. and Heaton, R. E., 1989, Static deformations from point sources and force couples located in welded elastic Poissonian half-spaces: Implications for seismic moment tensors, *Bulletin of the Seismological Society of America*, **79**(3), 813–841.

Hisada, Y., Bao, H., Bielak, J., Ghattas, O., and O'Hallaron, D., 1998, Simulations of long-period ground motions during the 1995 Hyogo-Ken Nanbu (Kobe) earthquake using a 3-D finite element method, *2nd International Symposium on Effect of Surface Geology on Seismic Motion*, Yokohama, Japan, 59–66.

Huang, B., Chen, K., Huang, W., Wang, J., Chang, T., Hwang, R., Chiu, H., and Tsai, C., 2000, Characteristics of strong ground motion across a thrust fault tip from the September 21, 1999, Chi-Chi, Taiwan earthquake, *Geophysical Research Letters*, **27**(17), 2729–2732.

Husseini, M., 1977, Energy balance for motion along a fault, *The Geophysical Journal of the Royal Astronomical Society*, **49**(3), 699–714.

ICBO, 1997, *Uniform Building Code*, International Conference of Building Officials (ICBO), Whittier, CA.

Inoue, T. and Miyatake, T., 1998, 3-D simulation of near-field strong ground motion based on dynamic modeling, *Bulletin of the Seismological Society of America*, **88**(6), 1445–1456.

Iwan, W. and Chen, X., 1994, Important near-field ground motion data from the Landers earthquake, *Proceedings of the 10th European Conference on Earthquake Engineering*, Vienna.

Kamae, K. and Irikura, K., 1998, Source model of the 1995 Hyogo-Ken Nanbu earthquake and simulation of near-source ground motion, *Bulletin of the Seismological Society of America*, **88**(2), 400–412.

Kanamori, H. and Heaton, T. H., 2000, Microscopic and macroscopic physics of earthquakes, J. B. Rundle, ed., *Geocomplexity and the Physics of Earthquakes*, **120**, 147–163, American Geophysical Union, Washington, DC.

Mikumo, T. and Miyatake, T., 1993, Dynamic rupture processes on a dipping fault, and estimates of stress drop and strength excess from the results of wave-form inversion, *Geophysical Journal International*, **112**(3), 481–496.

Oglesby, D. D., Archuleta, R. J., and Nielsen, S. B., 1998, Earthquakes on dipping faults: The effect of broken symmetry, *Science*, **280**(5366), 1055–1059.

Oglesby, D. D., Archuleta, R. J., and Nielsen, S. B., 2000a, Dynamics of dip-slip faulting: Explorations in two dimensions, *Journal of Geophysical Research - Solid Earth*, **105**(B6), 13643–13653.

Oglesby, D. D., Archuleta, R. J., and Nielsen, S. B., 2000b, The three-dimensional dynamics of dipping faults, *Bulletin of the Seismological Society of America*, **90**(3), 616–628.

Olsen, K. and Archuleta, R., 1996, Three-dimensional simulation of earthquakes on the Los Angeles fault system, *Bulletin of the Seismological Society of America*, **86**(3), 575–596.

Olsen, K., Madariaga, R., and Archuleta, R., 1997, Three-dimensional dynamic simulation of the 1992 Landers earthquake, *Science*, **278**, 834–839.

Pitarka, A., Irikura, K., Iwata, T., and Sekiguchi, S., 1998, Three-dimensional simulation of the near-fault ground motion for the 1995 Hyogo-ken Nanbu (Kobe), Japan, earthquake, *Bulletin of the Seismological Society of America*, **88**(2), 428–440.

Rao, S. S., 1999, *The Finite Element Method in Engineering*, 3rd edition, Butterworth Heinemann, Boston, MA.

Saikia, C. K., 1993, Estimated ground motions in Los Angeles due to $M_W = 7$ earthquake on the Elysian thrust fault, *Bulletin of the Seismological Society of America*, **83**(3), 780–810.

Shi, B., Anooshehpoor, A., Brune, J. N., and Zeng, Y., 1998, Dynamics of thrust faulting: 2-D lattice model, *Bulletin of the Seismological Society of America*, **88**(6), 1484–1494.

Spudich, P. and Frazer, L. N., 1984, Use of ray theory to calculate high-frequency radiation from earthquake sources having spatially variable rupture velocity and stress drop, *Bulletin of the Seismological Society of America*, **74**(6), 2061–2082.

Wald, D., 1996, Slip history of the 1995 Kobe, Japan, earthquake determined from strong motion, teleseismic, and geodetic data, *Journal of Physics of the Earth*, **44**(5), 489–503.

Wald, D., Helmberger, D., and Heaton, T., 1991, Rupture model of the 1989 Loma Prieta earthquake from the inversion of strong-motion and broadband teleseismic data, *Bulletin of the Seismological Society of America*, **81**(5), 1540–1572.

Wald, D. J. and Heaton, T. H., 1994, Spatial and temporal distribution of slip for the 1992 Landers, California, earthquake, *Bulletin of the Seismological Society of America*, **84**(3), 668–691.

Wald, D. J., Heaton, T. H., and Hudnut, K., 1996, The slip history of the 1994 Northridge, California, earthquake determined from strong-motion, teleseismic, GPS, and leveling data, *Bulletin of the Seismological Society of America*, **86**(1), S49–S70.

Wallace, R., 1984, Eyewitness account of surface faulting during the earthquake of 28 October 1983, Borah-Peak, Idaho, *Bulletin of the Seismological Society of America*, **74**(3), 1091–1094.

Yomogida, K. and Nakata, T., 1994, Large slip velocity of the surface rupture associated with the 1990 Luzon earthquake, *Geophysical Research Letters*, **21**(17), 1799–1802.